PR12-14-006

Initial State Helicity Correlation in Wide Angle Compton Scattering

A Proposal to Jefferson Lab PAC 42

D. Nikolenko, I. Rachek, Yu. Shestakov
Budker Institute, Novosibirsk, Russia

G.B. Franklin, V. Mamyan, B. Quinn
Carnegie Mellon University, Pittsburgh, PA 15213

T. Averett, M. Cummings, C. Perdrisat, H. Yao
College of William and Mary, Williamsburg, VA 23185

M. Huang, Z. Ye,
Duke University, Durham, NC 27708

C. Chen, E. Christy, N. Kalantarians, M. Kohl, Nuruzzaman
Hampton University, Hampton, VA 23668

G. Ron
Hebrew University of Jerusalem, Israel

N. Kivel
Helmholtz-Institut Mainz, Germany

C. Muñoz Camacho
Institut de Physique Nucleaire d'Orsay, IN2P3, BP 1, 91406 Orsay, France

J. Beričič, M. Mihovilovič, S. Štajner
J. Stefan Institute and Dept. of Physics, University of Ljubljana, Slovenia

W. Boeglin, P. Markowitz
Florida International University, Miami, FL 33199

J. Dunne, D. Dutta, M.H. Shabestari, L. Ye
Mississippi State University, Mississippi State, MS 39762

V. Punjabi
Norfolk State University, Norfolk, VA 23504

A. Ahmidouch, S. Danagoulian
North Carolina A&T State University, Greensboro, NC 27411

M. Amaryan, G. Dodge, L. El Fassi, C.E. Hyde, A. Radyushkin,
L. Weinstein
Old Dominion University

R. Gilman, K. Myers, R. Ransome
Rutgers, The State University of New Jersey, Piscataway, NJ 08854

E. Piasetzky
Tel Aviv University, Israel

A. Lukhanin, Z.-E. Meziani
Temple University, Philadelphia, PA 19122

I. Albayrak, T. Horn, F. Klein
The Catholic University of America, Washington DC, 20064

A. Camsonne, J. P. Chen, E. Chudakov, J. Gomez, D. Gaskell, O. Hansen,
D. W. Higinbotham, M. Jones, C. Keppel, D. Mack, R. Michaels, B. Sawatzky,
G. Smith, S. Wood
Thomas Jefferson National Accelerator Facility, Newport News, VA 23606

J. R. M. Annand, D. I. Glazier, D. G. Ireland,
I. J. D. MacGregor, B. McKinnon, B. Seitz, D. Sokhan
University of Glasgow, Glasgow, Scotland

T. Badman, E. Long, K. Slifer, P. Solvignon, R. Zielinski
University of New Hampshire, Durham, NH 03824

G. Cates, D. Crabb, D. Day(spokesperson), N. Dien,
C. Gu, D. Keller(spokesperson, contact), R. Lindgren, J. Liu,
N. Liyanage, V. Nelyubin, P. Peng, O. Rondon, M. Yurov
J. Zhang(spokesperson)
University of Virginia, Charlottesville, VA 22904

G. Miller
University of Washington, WA 98195

P. Kroll
University of Wuppertal, North Rhine-Westphalia, Germany

A. Asaturyan, A. Mkrtchyan, H. Mkrtchyan, A. Shahinyan, V. Tadevosyan,
H. Voskanyan, S. Zhamkochyan
Yerevan Physics Institute, Yerevan 0036, Armenia

The Neutral Particle Spectrometer collaboration
`https://wiki.jlab.org/cuawiki/index.php/Collaboration`

June 2, 2014

Contents

Abstract

We propose[1] an experiment to measure the initial state helicity correlation asymmetry A_{LL} in Real Compton Scattering (RCS) by scattering longitudinally polarized photons from a longitudinally polarized proton target at the invariant s= 8 (GeV/c)^{2}for three scattering angles, θ_γ^{cm} = 60°, 90° and 136°. This experiment could potentially run with the b_1 experiment (PR12-13-011) to make use of the very similar target setup already in place.

Two JLab RCS experiments, E99-114 and E07-002, demonstrated the feasibility of the experimental technique. The experiment utilizes an untagged bremsstrahlung photon beam and the UVA/JLAB polarized target. The scattered photon is detected in the future NPS. The coincident recoil proton is detected in the Hall C magnetic spectrometer HMS.

The applicability of QCD, in the moderate energy range, to exclusive reactions is a subject of great interest and any opportunity to test unambiguously its prediction should be taken.

Calculations by G. A. Miller in a constituent quark model reproduced the K_{LL} experimental result but revealed a large disagreement with the GPD prediction for A_{LL}. It is but one of the goals of our proposal to test this prediction which could force a modification of our understanding of the high-t photo-induced processes such as RCS, pion photoproduction, and deuteron photo–disintegration. A measure of $A_{LL}$and the conclusions that can be drawn from the results would give insight into understanding quark orbital angular momentum in the proton.

We request 742 hours of 90 nA at 4.4 GeV electron beam to measure the polarization observable A_{LL} to a statistical accuracy better than 0.09. This measurement will significantly increase our experimental confidence in the application of the GPD approach to reactions induced by real photons which will play a major role in nucleon structure physics at JLab.

[1]This is a resubmission of a previously approved experiment, E-05-101, that was scheduled to follow SANE in 2009, but delays in the schedule (largely budget driven) did not allow it to run

1 Introduction

Significant progress has been made over the last decade in our understanding of exclusive reactions in the hard scattering regime. This progress had been made possible (in part) by data from Jefferson Lab on elastic electron scattering and Compton scattering from the proton and by a significant and increasingly sophisticated theoretical effort to exploit the richness of exclusive reactions at moderate momentum transfers.

The observation of scaling in Deep Inelastic Scattering (DIS) at relatively low momentum transfers, successfully understood within the framework of pQCD, suggested that the same interpretation would be fruitful when applied to exclusive reactions: elastic electron scattering, photo- and electro-production of mesons, and Compton scattering. This prospect was further supported by the fact that constituent counting rules [1, 2], which naturally govern reactions that conform to the pQCD picture, could describe certain exclusive reactions.

There is little doubt that the pQCD mechanism dominates at high energies. What has been lacking is a general agreement as to how high the energy must be for pQCD to be completely applicable. The argument on this point is driven by more than a difference of (theoretical) opinion. The unavoidable fact is that cross sections calculated in a pQCD framework have invariably been low when compared to data, sometimes by an order of magnitude or more[3, 4].

Results of experiments at Jefferson Lab on the proton contradict the predictions of pQCD: the recoil polarization measurements of G_E^p E93-027, E04-108 and E99-007, and the Real Compton Scattering (RCS) experiment E99-114. The G_E^p measurements [5, 6, 7] found that the ratio of F_2 and F_1, scaled by Q^2 demands a revision of one of the precepts of pQCD, namely hadron helicity conservation. Results from the RCS measurement [8] are that the longitudinal polarization transfer K_{LL} is large and positive, also contrary to the pQCD predictions which find $K_{LL}$to be small and negative. These two experiments provide a compelling argument that pQCD should not be applied to exclusive processes at energy scales of 5-10 GeV.

Fortunately, an alternate theoretical framework exists for the interpretation of exclusive scattering at intermediate energies [9, 10, 11, 12]. This alternative approach asserts the dominance of the handbag diagram in which the reaction amplitude factorizes into a subprocess involving a hard interaction with a *single quark*. The coupling of the struck quark to the spectator system is described by the Generalized Parton Distributions (GPD's) [13, 14]. Since the GPD's are independent of the particular hard scattering reaction, the formalism leads to a unified description of hard exclusive reactions. Moreover, the relationship between GPD's and the normal parton distribution functions provides a natural framework for relating inclusive and exclusive reactions.

The RCS experiment E99-114 produced an especially remarkable result; not only was the measurement of K_{LL} inconsistent with pQCD, it was found that the longitudinal polarization is nearly as large as that expected for scattering from a free quark.

The QCD factorization approach formulated in the framework of Soft Collinear Effective Theory (SCET) can be used to develop a description of the soft-spectator scattering contribution [15, 16]. Recently a derivation of the complete factorization for the leading power contribution in wide angle Compton scattering has been worked out in the soft collinear effective theory. As factorization evolves and becomes less dependent on the assumption of restricted parton virtualities and parton transverse momenta RCS should receive the same level of attention that DVCS has. RCS have a complementary nature to DVCS in so far as in DVCS the GPDs are probed at small t while for RCS (and nucleon form factors) the GPDs are probed at large t.

A formalism for the RCS process based on the Dyson-Schwinger Equation (DSE) approach has been proposed by G. Eichmann and C. Fisher [17]. The specific results for the WACS observables in this framework are not yet published.

The initial state helicity correlation can be used to probe a theoretical model in detail. According to the handbag approach their angle dependence is close to that of the subprocess $\gamma q \to \gamma q$ diluted by form factors which take into account that the proton is a bound state of quarks and which represent $1/x$ moments of GPDs. The electromagnetic nucleon form factors have been revised using the generalized parton distributions analysis by M. Diehl and P. Kroll [18]. The various theoretical efforts made to apply the handbag approach to wide angle compton scattering (WACS) have produced predictions for its polarization observables including K_{LL} and A_{LL} [11, 19]. We must emphasize that the results of E99-114 are at a single kinematic point of a single observable. It is essential to verify the dominance of the handbag mechanism in other observables such as A_{LL}. In a recent development [19], a calculation of Miller suggests that a measurement of A_{LL} in WACS would be a test of perturbative chiral symmetry and of the mass of the quarks participating in the hard scattering.

There is much theoretical interest in WACS but a bit less activity at present which is only due to the lack of new data. The polarized observables are essential for moving the framework forward. There was only one polarization measurement of K_{LL} made during E99-114, so a similar experiment (E07-002) [20] at higher s was undertaken in Hall C to acquire three more K_{LL} points, the analysis of which is nearing completion. The next step is to obtain the K_{LL} complement by measuring the initial state helicity correlation asymmetry A_{LL} using a polarized proton target. We therefore propose a measurement of the polarization observable A_{LL} in Compton scattering at an incident energy of 4.4 GeV.

The proposal is organized as follows. In Section 2 we describe in more detail the handbag formalism and the predictions for RCS, some results from E99-114, and a summary of the physics goals of the proposed experiment. In Section 3 we describe the experimental approach and both the standard and the specialized equipment. In subsequent sections, we present our proposed measurements (Sec. 4), our expected results and beam time request (Sec. 5). Finally, the proposal is summarized in Section 8.

2 Physics Motivation

2.1 Overview

In view of the remarks in the Introduction, we consider several interesting questions that motivate us to explore further the measurement of polarization observables in RCS at JLab:

1. What is the nature of the quark which absorbs and emits photons in the RCS process in the wide angle regime? Is it a constituent or a current quark?

2. If the GPD approach is correct, is it indeed true that the RCS reaction proceeds through the interaction of photons with a single quark?

3. What are the constraints on the GPD integrals imposed from the proposed measurement of the A_{LL} observable?

In order to present a framework for addressing these issues, we next briefly discuss WACS in the soft-collinear effective theory, the handbag mechanism in the GPD conceptualization, and the handbag mechanism in the constituent quark model.

2.2 Soft-collinear Effective Theory

Recently a complete factorization formula for the leading power contribution in wide angle Compton scattering has been developed [15, 16]. The soft-spectator contribution describes the scattering which involves the soft modes and resulting soft-spectator scattering contribution to the overall amplitude. The soft collinear effective theory is used in order to define this contribution in a field theoretical approach. The SCET framework is then used to provide a proof of the factorization formula.

The SCET framework permits the implementation of some specific corrections which are related to the soft-overlap contribution. There are indications that numerical effect of this contribution can be dominant at some moderate values of the Mandelstam variables. In general, SCET give a very solid description in the region where the other power corrections are small.

The SCET formalism follows the same idea as in the standard factorization approach, short and long distance physics are factorized separately. The only required assumptions are very general such as that soft partons have soft momenta of order Λ_{qcd}. There is not an additional need to constrain the virtualities by hand. The advantage of SCET formalism is a systematic approach to the factorization of the hard and soft subprocesses.

The asymmetry K_{LL} is studied with the approximation that the hard-spectator contributions are small. Neglecting all power corrections and using the next-to-leading expressions some numerical results as a function of the scattering angle θ are obtained (see Fig.1). The solid red line corresponds to the leading-order approximation. The dashed (blue) and dotted

(black) lines show the numerical results for the complete NLO expression for the energies $s = 6.9$ GeV^2 and $s = 20$ GeV^2, respectively. The data point is from E99-114 and corresponds to $s = 6.9$ GeV^2. The value of the longitudinal asymmetry K_{LL} is qualitatively different from the one that can be obtained in the hard-spectator (hard two-gluon exchange) factorization picture.

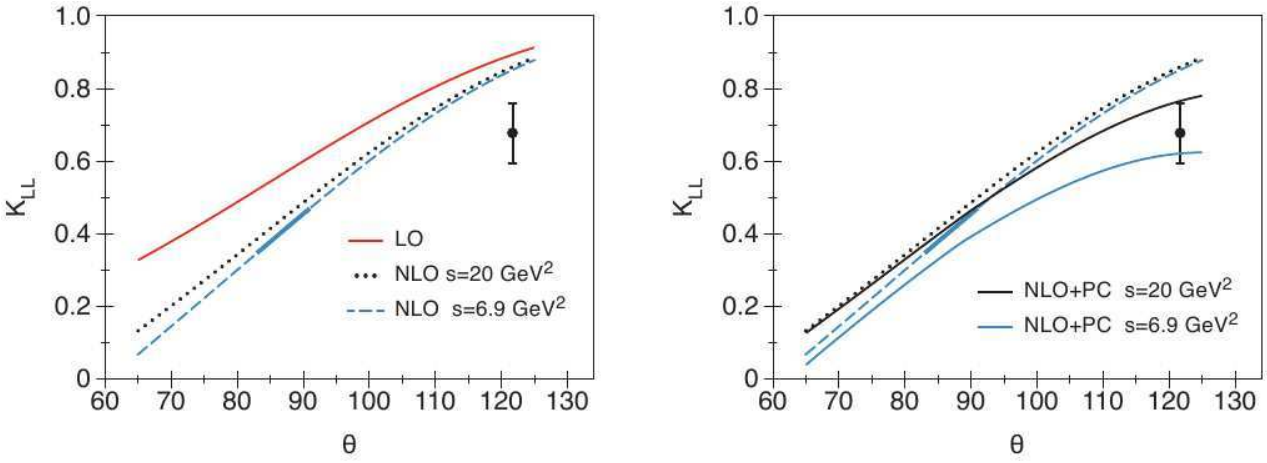

Figure 1: The longitudinal asymmetry K_{LL} as a function of scattering angle θ. (Left) A comparison of the LO (red) and NLO calculated with $s = 6.9$ GeV^2 (dashed) and $s = 20$ GeV^2 (dotted) lines. (Right) A comparison of the NLO results calculated with (solid black) and without (blue line) kinematical power corrections. The massless approximation is the same for both plots [16].

It is very relevant to describe a factorization for the helicity flip amplitudes but the modeling will be dependent on the new unknown nonperturbative matrix elements. Any experimental data on A_{LL} directly can provide the needed information to move forward in the acquisition of these nonperturbative quantities.

2.3 pQCD Mechanism

The traditional framework for the interpretation of hard exclusive reactions in the asymptotic regime is perturbative QCD (pQCD) [21, 22]. The onset of scaling in Deep Inelastic Scattering (DIS) at the relative low scale of $Q^2 \sim 1$–2 (GeV/c)^2, gives rise to the expectation that pQCD might also be applicable to exclusive processes in the range of a few (GeV/c)^2. pQCD confronts RCS [23, 24, 3] as shown in Fig. 2, where it is seen that the three valence quarks are active participants in the hard subprocess, which is mediated by the exchange of two hard gluons. The soft physics is contained in the valence quark distribution amplitudes. The pQCD mechanism leads naturally to the constituent counting rules for exclusive processes:

$$\frac{d\sigma}{dt} = \frac{f(\theta_{cm})}{s^n}, \quad (1)$$

where n is related to the number of active constituents in the reaction and $f(\theta_{cm})$ is a function only of the center of mass scattering angle[1, 2]. Indeed, the observation that many exclusive reactions, such as elastic electron scattering, pion photoproduction, and RCS, approximately obey Eq. 1 has led to the belief that the pQCD mechanism dominates at experimentally accessible energies. There seems to be little theoretical disagreement that the pQCD mechanism dominates at sufficiently high energies [21]; however, there is no consensus on how high is "sufficiently high." Despite the observed scaling, absolute cross sections calculated using the pQCD framework are very often low compared to existing experimental data, sometimes by more than an order of magnitude [3, 4]. Moreover, several recent JLab experiments that measure polarization observables also disagree with the predictions of pQCD. In the G_E^p experiment [5, 6, 7] the slow falloff of the Pauli form factor $F_2(Q^2)$ up to Q^2 of 8.5 $(\mathrm{GeV}/c)^2$ provides direct evidence that hadron helicity is not conserved, contrary to predictions of pQCD. Similar findings were made in the π^0 photoproduction experiment [25], where both the non-zero transverse and normal components of polarization of the recoil proton are indicative of hadron helicity-flip, which is again contrary to the predictions of pQCD. Finally, in the recently completed RCS experiment, E99-114 (new data will also soon be available from E07-002), the longitudinal polarization transfer K_{LL} (which will be defined precisely in the next section) shows a value which is large and positive, contrary to the pQCD prediction which is small and negative [3]. For all these reasons, it can be argued that pQCD is not the correct mechanism for interpreting exclusive reactions at currently accessible energies and instead we should seek a description in terms of the handbag mechanism. The pQCD calculations predict that A_{LL}=K_{LL}, so a measurement of A_{LL} in combination with the already obtained result for K_{LL} could provide an additional test of pQCD applicability in the JLab energy regime.

2.4 Handbag Mechanism

The handbag mechanism offers new possibilities for the interpretation of hard exclusive reactions. For example, it provides the framework for the interpretation of deep exclusive reactions, which are reactions initiated by a high-Q^2 virtual photon. The application of the formalism to RCS (see Fig. 3) was initially worked out to leading order (LO) by Radyushkin [9] and subsequently by Diehl *et al.*[10]. The next-to-leading-order (NLO) contributions have been worked out by Huang *et al.*[11]. The corresponding diagram for elastic electron scattering is similar to Fig. 3, except that there is only one external virtual photon rather than two real photons. In the handbag approach, the hard physics is contained in the

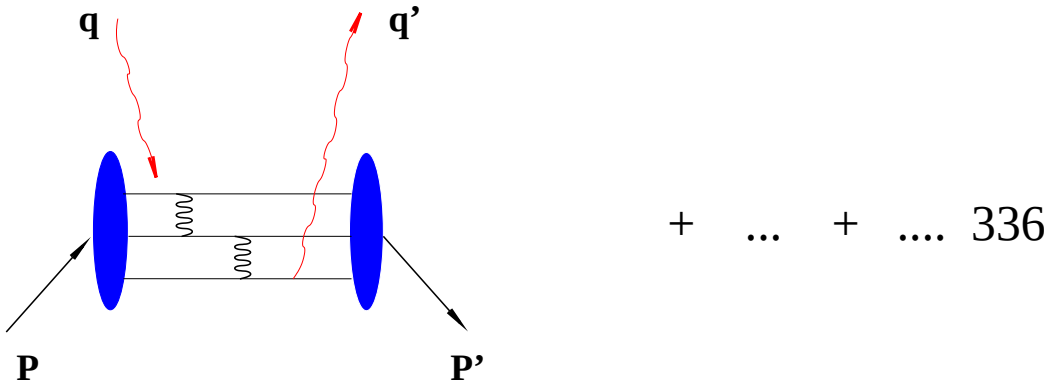

Figure 2: Two gluon exchange pQCD diagram for RCS. 336 diagrams can contribute.

scattering from a single active quark and is calculable using pQCD and QED: it is just Compton scattering from a structureless spin-1/2 particle.

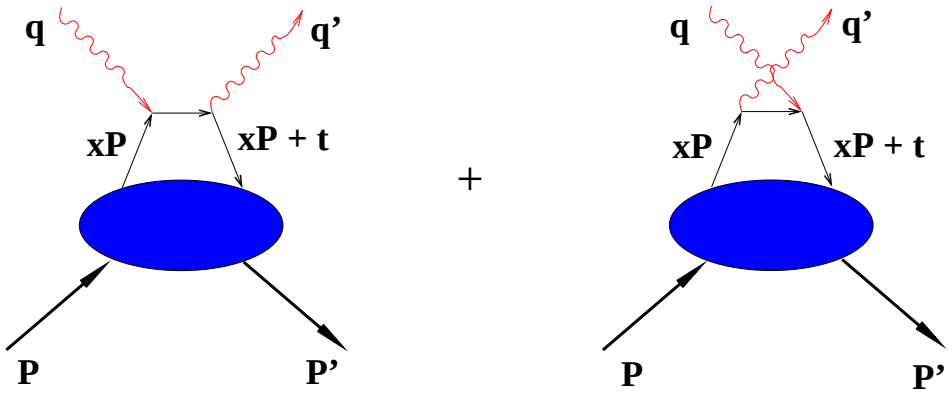

Figure 3: The handbag diagram for RCS.

The soft physics is contained in the wave function describing how the active quark couples to the proton. This coupling is described in terms of GPD's. The GPD's have been the subject of intense experimental and theoretical activity [13, 14]. They represent "superstructures" of the proton, from which are derived other measurable structure functions, such as parton distribution functions (PDF) and form factors (F_1 and F_2). To NLO, only three of the four GPD's contribute to the RCS process: $H(x, \xi = 0, t)$, $\hat{H}(x, \xi = 0, t)$, and $E(x, \xi = 0, t)$. Since the photons are both real, the skewness parameter ξ is zero, reflecting the fact that the momentum absorbed by the struck quark is purely transverse. In the handbag formalism, the RCS observables are new form factors of the proton that are x^{-1}-moments of the GPD's:

$$
\begin{aligned}
R_{_V}(t) &= \sum_a e_a^2 \int_{-1}^{1} \frac{dx}{x} H^a(x,0,t), \\
R_{_A}(t) &= \sum_a e_a^2 \int_{-1}^{1} \frac{dx}{x} \,\mathrm{sign}(x)\, \hat{H}^a(x,0,t), \\
R_{_T}(t) &= \sum_a e_a^2 \int_{-1}^{1} \frac{dx}{x} E^a(x,0,t),
\end{aligned}
$$

where e_a is the charge of the active quark and the three form factors are, respectively, the vector, axial vector, and tensor form factors. ($\mathrm{sign}(x)$ is the sign of x $\equiv \frac{x}{|x|}$.) The corresponding form factors for elastic electron or neutrino scattering are given by the first (x^0) moments of the same GPD's:

$$
\begin{aligned}
F_{_1}(t) &= \sum_a e_a \int_{-1}^{1} dx\, H^a(x,0,t), \\
G_{_A}(t) &= \sum_a \int_{-1}^{1} dx\, \mathrm{sign}(x)\, \hat{H}^a(x,0,t), \\
F_{_2}(t) &= \sum_a e_a \int_{-1}^{1} dx\, E^a(x,0,t),
\end{aligned}
$$

where the three quantities are, respectively, the Dirac, axial, and Pauli form factors. On the other hand, the $t = 0$ limit of the GPD's produce the PDF's:

$$
\begin{aligned}
H^a(x,0,0) &= q^a(x), \\
\hat{H}^a(x,0,0) &= \Delta q^a(x) \\
E^a(x,0,0) &= 2\frac{J^a(x)}{x} - q^a(x),
\end{aligned} \tag{2}
$$

where J^a is the total angular momentum of a quark of flavor a and is not directly measurable in DIS.

In the handbag factorization scheme, the RCS helicity amplitudes are related to the form factors by

$$
\begin{aligned}
M_{\mu'+,\mu+}(s,t) &= 2\pi\alpha_{em}\left[T_{\mu'+,\mu+}(s,t)(R_{_V}(t) + R_{_A}(t)) + T_{\mu'-,\mu-}(s,t)(R_{_V}(t) - R_{_A}(t))\right], \\
M_{\mu'-,\mu+}(s,t) &= 2\pi\alpha_{em}\frac{\sqrt{-t}}{m}\left[T_{\mu'+,\mu+}(s,t) + T_{\mu'-,\mu-}(s,t)\right] R_{_T}(t),
\end{aligned}
$$

where μ, μ' denote the helicity of the incoming and outgoing photons, respectively. The signs on M and T refer to the helicities of the proton and active quark, respectively. This structure

of the helicity amplitudes leads to a simple interpretation of the RCS form factors: $R_V \pm R_A$ is the response of the proton to the emission and reabsorption of quarks with helicity in the same/opposite direction of the proton helicity, and R_T is directly related to the proton helicity-flip amplitude [11]. These equations leads to expressions relating RCS observables to the form factors.

The most important of these experimentally are the spin-averaged cross section, the recoil polarization observables and A_{LL}. The spin-averaged cross section factorizes into a simple product of the Klein-Nishina (KN) cross section describing the hard scattering from a single quark, and a sum of form factors depending only on t [9, 10]:

$$\frac{d\sigma/dt}{d\sigma_{\rm KN}/dt} \;=\; f_V \left[R_V^2(t) \;+\; \frac{-t}{4m^2} R_T^2(t)\right] + (1-f_V) R_A^2(t)\,. \tag{3}$$

For the interesting region of large $p_\perp$, the kinematic factor f_V is always close to 1. Consequently the unpolarized cross sections are largely insensitive to R_A, and the left-hand-side of Eq. 3 is nearly s-independent at fixed t. One of the primary goals of E99-114 was to test this relationship as well as to determine the vector form factor R_V. Calculations to NLO, which take into account both photon and proton helicity-flip amplitudes, do not change this prediction in any appreciable way [11, 26]. Updated cross section and Compton form factors (see Fig. 4) with their parametric uncertainties have also been evaluated [18].

The longitudinal and transverse polarization transfer observables, K_{LL} and K_{LS}, respectively, are defined by

$$K_{LL}\frac{d\sigma}{dt} \;\equiv\; \frac{1}{2}\left[\frac{d\sigma(\uparrow\uparrow)}{dt} - \frac{d\sigma((\downarrow\uparrow)}{dt}\right] \qquad K_{LS}\frac{d\sigma}{dt} \;\equiv\; \frac{1}{2}\left[\frac{d\sigma(\uparrow\rightarrow)}{dt} - \frac{d\sigma(\downarrow\rightarrow)}{dt}\right] \tag{4}$$

where the first arrow refers to the incident photon helicity and the second to the recoil proton helicity ($\uparrow$) or transverse polarization ($\rightarrow$).

With definitions of two additional parameters,

$$\beta \;=\; \frac{2m}{\sqrt{s}}\,\frac{\sqrt{-t}}{\sqrt{s}+\sqrt{-u}} \qquad \kappa(t) \;=\; \frac{\sqrt{-t}}{2m}\,\frac{R_T(t)}{R_V(t)}\,, \tag{5}$$

the three polarization observables are approximately related to the form factors by the expressions [10, 11],

$$K_{LL} \;\approx\; K_{LL}^{\rm KN}\,\frac{R_A(t)}{R_V(t)}\,\frac{1-\beta\kappa(t)}{1+\kappa^2(t)} \qquad \frac{K_{LS}}{K_{LL}} \;\approx\; \kappa(t)\,\frac{1+\beta\kappa^{-1}(t)}{1-\beta\kappa(t)} \qquad P_N \;\approx 0\,, \tag{6}$$

where $K_{LL}^{\rm KN}$ is the longitudinal asymmetry for a structureless Dirac particle. These formulas do not include small gluonic corrections, which are discussed in Ref. [11].

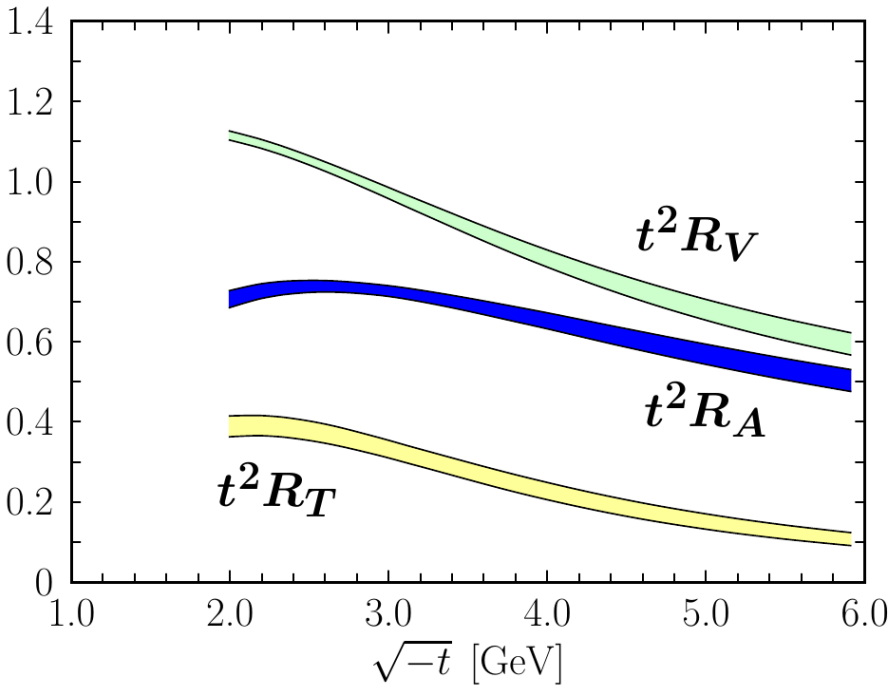

Figure 4: Predictions for the Compton form factors evaluated from the M. Diehl, P. Kroll default fit from Ref. [11], scaled by t^2 and shown in units of GeV^4. The bands in each case show the parametric uncertainties.

The expressions above show that measurements of K_{LL} and K_{LS}, when combined with measurements of $d\sigma/dt$, allow determinations of all three form factors. They also show that two very important pieces of information follow directly from the spin asymmetries: K_{LL} and K_{LS} / K_{LL}, which are directly related to the form factor ratios R_A/R_V and R_T/R_V, respectively.

The initial state helicity correlation parameter is defined by,

$$A_{LL}\frac{d\sigma}{dt} \equiv \frac{1}{2}\left[\frac{d\sigma(\uparrow\uparrow)}{dt} - \frac{d\sigma((\downarrow\uparrow)}{dt}\right] \tag{7}$$

where the first arrow refers to the incident photon helicity and the second to the initial state proton helicity ($\uparrow$). In the GPD approach of Ref. [11], the initial state helicity correlation parameter, A_{LL}, equals K_{LL} so all the predicted relationships between A_{LL} and the RCS form factors are the same as shown above for K_{LL}.

From the relationships (Eq. 2) connecting the RCS form factors to PDFs, the ratio R_A/R_V is related to $\Delta q^a(x)/q^a(x)$. For RCS, the e_a^2-weighting of the quark flavors means

that u quarks will dominate the reaction. Moreover, at relatively large $-t$, the contributions to the form-factor integral are concentrated at moderate-to-high x, where the valence quarks dominate. Therefore, the A_{LL} asymmetry contains direct information on $\Delta u(x)/u(x)$ in the valence region. We propose to investigate this in the present experiment, up to $-t = 5.4$ $(\mathrm{GeV}/c)^2$.

Obtaining this kind of information is one of the key physics elements justifying the 12 GeV upgrade of JLab. From the correspondence between RCS and electron scattering form factors, there is expected to be a close relationship between R_T/R_V and F_2/F_1 [11]. The measurements of G_E^p at JLab [5, 6, 7] have shown that F_2/F_1 falls as $1/\sqrt{-t}$ rather than as $1/t$, the latter being predicted by pQCD. It will be an important check on the theoretical interpretation of F_2/F_1 to see if R_T/R_V behaves in a similar way. The results from E99-114 at $-t = 4$ are large but suggest that the R_T/R_V may fall more rapidly with $-t$ than F_2/F_1. Experiment E07-002 is expect to obtain better precision on K_{LT} and K_{LL} leading to new results for the relationship between F_2/F_1 and R_T/R_V. These results must be compared with the R_T/R_V acquired with the A_{LL} asymmetry. This will serve as a consistency check if K_{LL} and A_{LL} are equal, but serve as a phenomenological basis if they are not. It is expected that significant model sensitivities occur in beam-target double-polarization asymmetries, these could be measured with much higher efficiency than ones requiring recoil polarization determination.

2.5 Relativistic constituent quark model for RCS

The relativistic constituent quark model developed by G. A. Miller [19] addresses the question of what is the dominant reaction mechanism that allows the proton to accommodate the large momentum transfer in exclusive reactions such as elastic electron and photon scattering. This model has been successful in describing the electromagnetic nucleon form factors [27]. Unlike the handbag calculations within the GPD approach [10, 11], Miller's model does not neglect quark and hadron helicity flip. The model starts with a wave function for three relativistic constituent quarks:

$$\Psi(p_i) = u(p_1)u(p_2)u(p_3)\psi(p_1, p_2, p_3),$$

where p_i represents space, spin, and isospin indices. It evaluates the wave function in the light cone variables and the calculations are relativistic. They obey gauge invariance, parity conservation, and time reversal invariance. They include quark mass effects and proton helicity flip. Due to lower components of Dirac spinors, where the quark spin is opposite to that of the proton, quark orbital angular momentum appears. The resulting predictions for the polarization observables A_{LL} and K_{LL} and the cross section are shown in Fig. 5 and Fig. 6, together with data from the E99-114 experiment. The most striking consequence of Miller's results is a big difference between A_{LL} and K_{LL} at large scattering angles, which we can test experimentally.

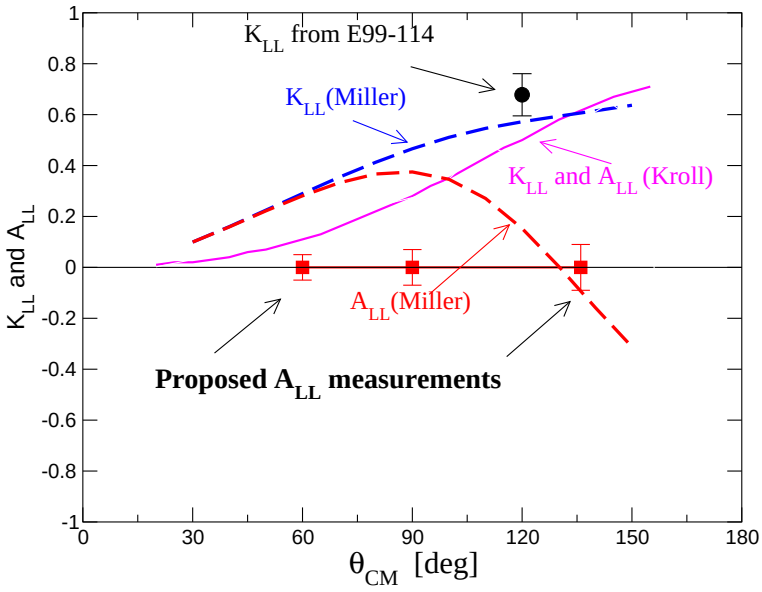

Figure 5: Predictions for A_{LL} in the GPD approach of Ref. [11] and CQM of Ref. [19] along with the data on K_{LL} from E99-114 and the expected precision of the proposed measurements.

2.6 Polarization in QED Compton process

It is instructive to evaluate polarization effects in the QED process $e\gamma \to e\gamma$. The Klein-Nishina process is an example that is fully calculable and which plays a major role in RCS, when the handbag diagram dominates. It is useful to evaluate polarization observables for different ratios of the electron mass to the photon energy.

Polarization observables in QED are given in invariant variables as [28] :

$$A_{LL}^{KN} = \left[-\frac{s-m^2}{u-m^2} + \frac{u-m^2}{s-m^2} - \frac{2m^2t^2(s-u)}{(s-m^2)^2(u-m^2)^2}\right] / \left[-\frac{s-m^2}{u-m^2} - \frac{u-m^2}{s-m^2} + \frac{4m^2t(m^4-su)}{(s-m^2)^2(u-m^2)^2}\right]$$

$$K_{LL}^{KN} = \left[-\frac{s-m^2}{u-m^2} + \frac{u-m^2}{s-m^2} - \frac{4m^2t^2(m^4-su)}{(s-m^2)^3(u-m^2)^2}\right] / \left[-\frac{s-m^2}{u-m^2} - \frac{u-m^2}{s-m^2} + \frac{4m^2t(m^4-su)}{(s-m^2)^2(u-m^2)^2}\right]$$

Fig. 7 shows the A_{LL}^{KN} and K_{LL}^{KN} for different energies of the incident photon as a function of the scattering angle in the *lab*. At low t/s and for $m/E_\gamma << 1$ the difference between K_{LL} and A_{LL} vanishes. At $\theta_{lab} = \pi/2$ the observable A_{LL}=0. In the limit $m/E_\gamma \to 0$ A_{LL}=K_{LL} for all values of θ_γ not equal to 180°. At $\theta_\gamma = 180°$ the value of $A_{LL} \approx -K_{LL}$. If we now look at Miller's calculation (see Figure 5) which has $m/E_\gamma \sim 1/10$ and $\theta_{lab} \approx 90°$ (our kinematics labeled P2, see Table 1) the difference between K_{LL} and A_{LL} is about 0.7.

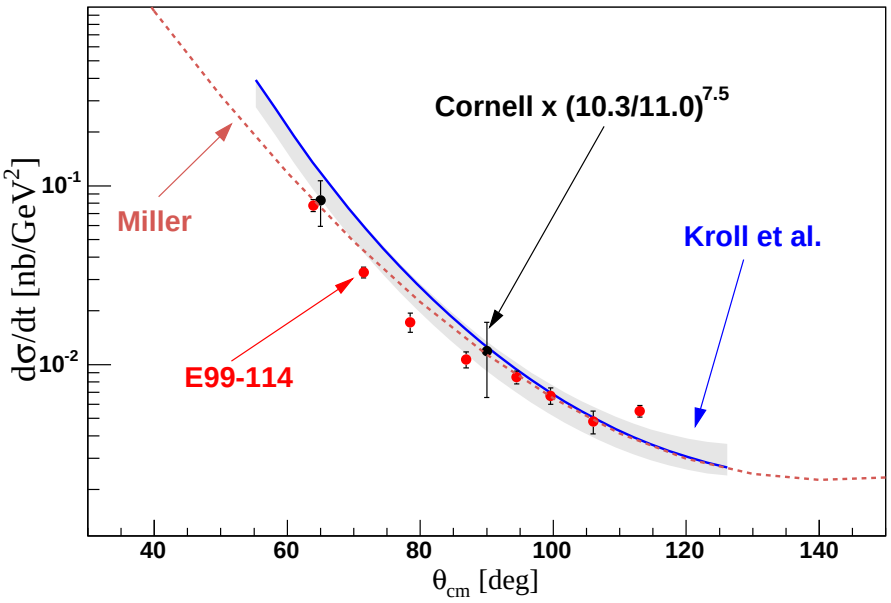

Figure 6: Cross section of RCS process at s = 11 $(\mathrm{GeV}/c)^2$ from E99-114 and Cornell[33] experiments (scaled to the same CM energy) and results of calculations in the GPD approach (Kroll) and from a CQM (Miller).

2.7 Regge Exchange Mechanism

When s, $-t$, and $-u$ are not sufficiently large, then the factorization into hard and soft process may not apply, in which case neither the pQCD nor the handbag approach is valid. An alternative approach has been proposed by Laget [12] based on Vector Meson Dominance (VMD). In the VMD approach, the photon fluctuates into a vector meson, which then interacts with the target via t-channel exchange of mesons (which dominates at low t or forward angles) or u-channel exchange of baryons (which dominates at low u or backward angles). The open question is how high t or u must be in order that the VMD mechanism becomes small compared to the handbag mechanism. The VMD model has had recent successes even at moderately large t. For example the VMD model is able to fit the observed low value of the G_E^p form factor [6] at -t = 5.6 $(\mathrm{GeV/c})^2$ [29].

Real and Virtual Compton Scattering were studied in a model based on Regge trajectories and two-gluon exchange by F. Cano and J.-M. Laget [12]. The parameters of the model were "tuned" by fitting data from vector meson photonproduction [30, 31], giving rise to predictions for the cross section and spin observables in RCS involving only a single free parameter, the radiative decay constant of the ρ meson. Given the close agreement over much of the kinematic range between the handbag and VMD predictions, they point out

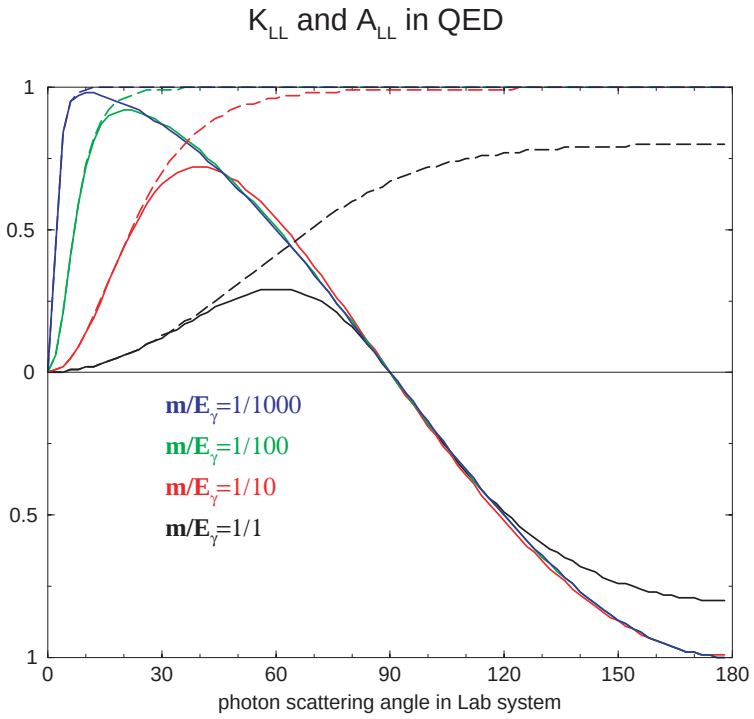

Figure 7: Klein-Nishina polarization observables A_{LL} and K_{LL}, shown by solid lines and dashed lines respectively, for different ratios of the electron mass to the photon energy as a function of the scattering angle in the lab system.

that at presently accessible momentum transfer, the contribution to RCS from the hadronic component of the photon is not negligible (see review [32]). For example the predicted longitudinal polarization transfer (see Fig. 8) $A_{LL}$is positive, close to the prediction of the handbag approach at θ^{cm} below 140°, and close to the result from E99-114. However, it strongly deviates from the handbag prediction at larger angles, where the u-channel exchange of baryons becomes dominant.

2.8 Additional Remarks

It is important to realize that the issues posed at the start of this section are not limited to the RCS reaction. Indeed, they are questions that need to be addressed by all studies of the proton using exclusive reactions in the hard scattering regime. The old paradigm for addressing these questions was the pQCD mechanism and the distribution amplitudes. It is quite likely that the new paradigm will be the handbag mechanism and GPD's. In any case, the reaction mechanism needs to be tested, not only over a wide range of kinematic variables

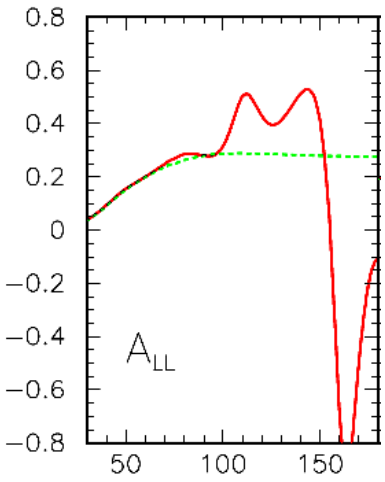

Figure 8: Prediction from [12] of A_{LL} in Compton Scattering at $E_\gamma = 4$ GeV. Dashed lines are the contribution of Regge Exchange in the t-channel. Solid lines are the final results, which include u-channel exchanges.

but also over a wide range of different reactions. Of these, RCS offers the best possibility to test the mechanism free of complications from additional hadrons. The CQM was quite successful in its description of many observables of the hadronic structure and generates a useful and intuitive picture of the hadron. The proposed test presents a unique case where predictions of the CQM and QCD–based theory are qualitatively different.

2.9 Support from Theory Community

During the preparation of this proposal, we contacted several theorists to gauge interest in a measurement of the initial state helicity correlation in WACS. The response was uniformly positive. We provide some of their feedback for context.

> I think it is very interesting to measure A_{LL}. It will be either close to or far from K_{LL}. Either result would have important implications for understanding quark orbital angular momentum in the proton. Jerry Miller

I am happy to learn that there is interest in RCS and am willing to support any activity of measuring A_{LL}. It is difficult to understand why there is still a lot of activity on DVCS at Jlab but not for RCS. There is a robust prediction for A_{LL} (and K_{LL}) in the handbag mechanism. It is given by the subprocess helicity correlation which is to be calculated from perturbation theory, diluted somewhat by the ratio of the phenomenological Compton form factors R_A and R_V. These form factors have been calculated from generalized parton distributions extracted from the nucleon form factors through the sum rules. Peter Kroll

WACS polarization measurements on the proton will be of great help for developing the theory since they are typically calculated with the same or slightly extended nonperturbative input as the unpolarized cross section. The physics situation has never been fully clarified. There may not be as much theoretical activity as a few years ago, which is not for lack of interest but due to the somewhat dormant situation regarding new data. Markus Diehl

I think that it is very important to measure A_{LL} in order to see directly the mechanism of the hard subprocess and to check theoretical predictions. N. Kivel

2.10 Summary of Physics Goals

We propose measurements of the spin correlation asymmetry A_{LL} at an incident photon energy of 4.4 GeV, s=8 (GeV/c)^2, at three scattering angles; at $\theta_\gamma^{cm} = 60^\circ$ corresponding to $-t$=-1.7 (GeV/c)^2, at $\theta_\gamma^{cm} = 90^\circ$ corresponding to $-t$=-3.3 and at $\theta_\gamma^{cm} = 136^\circ$ corresponding to $-t$=5.4 (GeV/c)^2. The specific physics goals are as follows:

1. To make a measurement of A_{LL} at large s, t and u where applicability and limitations of GPD based calculations are under control. A high precision measurement will support the surprising result from Hall A for K_{LL}[8] and complement the experiment E07-002 [20].

2. To provide a test that can expose, in an unambiguous way, how the RCS reaction proceeds: either via the interaction of photons with a current quark or, with a constituent quark.

3. To determine the form factor ratio R_A/R_V from the measurement of A_{LL} and correlate this ratio with the corresponding values of F_2/F_1 determined from elastic electron scattering.

The overall statistical precision with which we will address these physics goals will be discussed in Sec. 5.

3 Experimental Setup

The proposed experiment will study the scattering of polarized photons from a polarized hydrogen target, as illustrated in Fig. 9. The scattered photon will be detected by the Neutral Particle Spectrometer (NPS) installed at a distance to match the acceptance of the HMS, which will be used to detect the recoiling proton.

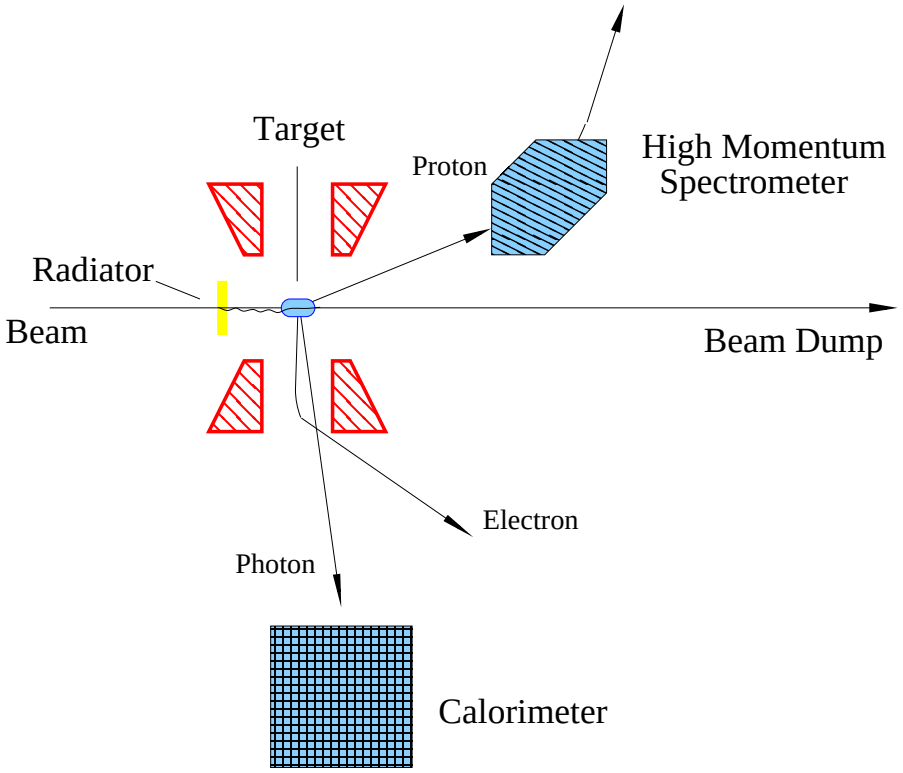

Figure 9: Schematic of the experimental setup. The target is longitudinally polarized (along the beam). The scattered photon is detected by NPS and the recoil proton is detected by the HMS. Teh scattered electron in the mixed photon-electron beam is deflected by the polarized target magnet.

We assume an incident electron beam of 4.4 GeV with intensity of 90 nA and 80% polarization. Such currents and polarizations have already been delivered using the strained GaAs source at Jefferson Lab before. The target will be a longitudinally polarized proton, which is the so called UVA/JLAB polarized target, operating in a 5 Tesla field pointing along the beam line (longitudinal). A sweeping magnet is not required since the target field will deflect the charged particles away from the NPS.

With this beam intensity on UVA/JLAB polarized target, a average NH_3 polarization of 75% have been achieved in several experiments, i.e. RSS, SANE experiments in Hall C, g_2^P

and G_E^P experiments in Hall A. The beam polarization will be measured with a systematic uncertainty of 2% with the Hall C Möller polarimeter. The large cross section and helicity asymmetry for π^0 photoproduction, as determined in E99-114, will provide a monitor of the electron beam polarization continuously during data taking at fixed kinematic conditions with large θ_γ^{cm}(See discussion in Section 4.3 on signal extraction).

3.1 The Polarized Hydrogen Target and the Radiator

In this experiment we will use the University of Virginia polarized target, which has been successfully used in E143/E155/E155x experiments at SLAC and E93-026, E01-006, E07-003, E08-007 and E08-027 at JLab. E08-007 and E08-027 used a different coil from Hall B, which is very similar to the original one except with larger openning. See Fig. 10 for a cross section view. We will polarized the target in longitudinal direction.

This target operates on the principle of Dynamic Nuclear Polarization (DNP). The low temperature (1 K°), high magnetic field (5 T) natural polarization of solid materials (ammonia, lithium hydrides) is enhanced by microwave pumping. The polarized target assembly contains two 3–cm–long target cells that can be selected individually by remote control to be located in the uniform field region of a superconducting Helmholtz pair. They are also 2 other target cells which are available for calibration target like carbon foil or CH_2. The permeable target cells are immersed in a vessel filled with liquid helium and maintained at 1 K by using a high power evaporation refrigerator. The magnet coils have a 55° conical shaped aperture along the axis and a 38° wedge shaped aperture along the vertically oriented midplane.

The target material, during the experiment, will be exposed to 140 GHz microwaves to drive the hyperfine transition which aligns the nucleon spins. The DNP technique produces proton polarizations of up to 95% in the NH_3 target. The heating of the target by the beam causes an initial drop of a few percent in the polarization. Then the polarization slowly decreases due to radiation damage. Most of the radiation damage is repaired by annealing the target at about 80 K, until the accumulated dose reaches $> 2 \times 10^{17}$ electrons, at which point the material needs to be changed. Due to limitations in the heat removal by the refrigerator, the luminosity (considering only the polarized material in the uniform field region) is limited to 85×10^{33} cm^{-2} Hz. As part of the program to minimize the sources of systematic errors, the target polarization direction will be reversed after each anneal by adjusting the microwave frequency.

A radiator will be mounted on the liquid nitrogen shield about 10 inches upstream of the target magnet center. The short distance between the target and radiator helps to avoid background produced from plastic target wall and downstream beam line. The separation of the events produced in the radiator is of order 5 cm (in the worst case) in the spectrometer y_{tg} coordinate, which is comfortably large compared to the y_{tg} resolution of 0.3 cm. We are going to use a copper radiator with thickness of 0.86 mm, which is 6% radiation length. Pair

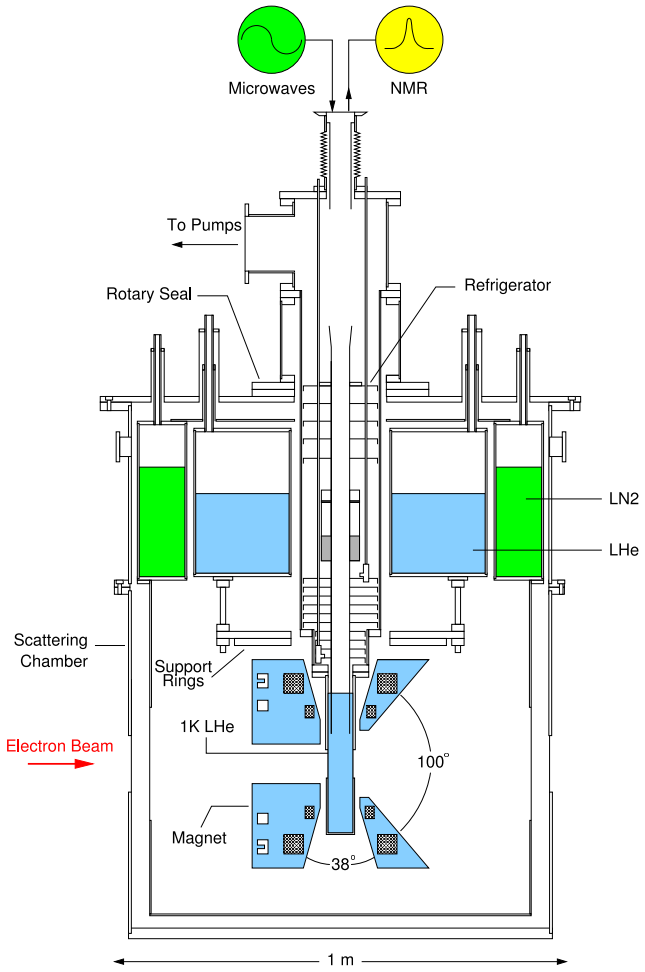

Figure 10: Cross section view of the polarized target.

production in the radiator will add 5.4% to the heat load of the refrigerator, so that the average beam current should be reduced by 5.4% yielding a useful luminosity of 80×10^{33} cm^{-2} Hz.

The polarized target magnet will deflect outgoing charged particles in both the vertical and horizontal directions, which greatly improves the selection of the elastically scattered photons from the elastically scattered electrons at the calorimeter. The RCS experiment, E99-114, installed a sweep magnet between the target and the calorimeter to achieve similar result, but in their case the electrons were bent in the horizontal plane. Simulations show that bending charged particles (mainly electrons) vertically will yield a better signal to background ratio since it allows one to cut the uniform like background in both horizontal and vertical positions.

3.2 The Photon Detector

Participants in this experimental effort are also members of the Neutral Particle Spectrometer (NPS) collaboration who will build the NPS (See Appendix for details about the NPS) for this and other proposed experiments, for example, E12-13-010, E12-13-007 and unpolarized WACS experiments. The sensitive region of this calorimeter is 30 (horizontal) x 36 (vertical) inches, sitting on a frame allowing for easy movement. The position resolution of the NPS is 3 mm and the energy resolution, $\sigma_E/\sqrt{E}$, is better than 3%.

We plan to place the NPS in three locations. The forward angle position 22° (in the lab) serves two purposes: first to allow the calibration with elastically scattered electrons and also for production data taking at $\theta_{cm} = 60°$. The second position, 37°, is for production at $\theta_{cm} = 90°$. The 37° is chosen to optimize acceptance as well as being a direct overlap with the measurement of K_{LL}at $\theta_{cm} = 90°$ from experiment E07-002. In the Miller prediction $A_{LL}$and K_{LL}begin to diverge around this point (See Fig 5). This is also a critical point from the factorization standpoint due to the large Mandelstam variables where SCET and the handbag model are designed to describe WACS. The third position is 78° in the lab, which is for production running at $\theta_{cm} = 136°$. This is the essential point needed to cleanly differentiate between models. The spectrometer angle of the HMS, which detects the protons, will be adjusted for each kinematics to match the photon scattering angle. The distance from the target to the calorimeter is chosen to insure an adequate angular coverage of the calorimeter to match HMS.

3.3 Proton Polarization in the Target

Polarization of the target will be measured by NMR with an accuracy at the level of 4%. The P1 kinematics (see Table 1) will provide an opportunity for the independent determination of the proton polarization. In the P1 kinematics, scattered electrons will be deflected in the target by 1.7 degrees in the vertical direction, which leads to a vertical displacement of 23 cm at the front face of the calorimeter. For elastic electron proton scattering the beam–target asymmetry can be calculated from the following expression [36, 37]:

$$A^{ep} = \frac{2\sqrt{\tau(1+\tau)}\,\tan\frac{\theta}{2}}{g^2 + \tau\epsilon^{-1}} \cdot (g\,\sin\phi + \sqrt{\tau}\,\cos\phi) \tag{8}$$

where $g = G_E^p/G_M^p$ is the ratio of the proton form factors, θ is the scattering angle, $\tau = Q^2/4M_p^2$, (M_p is the proton mass), and $Q^2 = 4E_iE_f\sin^2\frac{\theta}{2}$, $E_{i(f)}$ is the initial (final) electron energy, $\epsilon^{-1} = 1 + 2(1+\tau)\tan^2\frac{\theta}{2}$ and $\sin\phi = \cos\frac{\theta}{2}/\sqrt{(1+E_i/M_p)(2+E_i/M_p)\sin^2\frac{\theta}{2}}$. This expression explicitly takes into consideration that the polarization axis is along the beam direction and in the scattering (horizontal) plane.

Through its measurement the product of the beam and the target polarization will be determined with a statistical accuracy of 0.02. This will provide an additional monitor of the beam and target polarization averaged over the duration of the data taking.

4 Proposed Measurements

An 80% longitudinally polarized electron beam with current of 90 nA at energy of 4.4 GeV will be used in the proposed experiment. A copper radiator with the thickness of 0.86 mm (6% radiation length) will be installed 10 inches upstream of the 3 cm NH_3 target, inside the scattering chamber. The circular polarization of the bremsstrahlung photon drops quickly as the photon energy decreasing. Their relationship is described by Eq. 9:

$$\frac{P_\gamma}{P_e} = \frac{4y - y^2}{4 - 4y + 3y^2}\,, \tag{9}$$

where $y = \frac{E_\gamma}{E_e}$ is the fraction of the photon energy to the electron beam energy. We optimized the detector acceptance to pick those photons that carry 80% to 95% of the incident electron energy. For such bremsstrahlung photons, the average circular polarization is about 97.6% of the polarization of the electrons. We will use HMS to detect the recoil proton. The scattered photon will be detected by the future Neutral Particle Spectrometer(NPS).

4.1 The Kinematics

Table 1 shows the kinematics parameters of the proposed experiment. The central momentum of the proton spectrometer is determined through a Geant4 simulation and optimized for the maximum acceptance for incident photon energy from 80% to 95% of the electron beam energies. The distance of the front face of NPS to the target center (L) and its vertical offset (H) are also optimized for maximum RCS acceptance through the simulation. The overlap of the acceptances of the photon and proton arms are chosen in a way such that the angular acceptance is defined by the proton arm. Because the target field also bend the outgoing proton, those protons detected by HMS have an out-of-plane-angle offset. This also cause the outgoing photon to have a compensating out-of-plane-angle offset. Therefore we have to shift the photon arm vertically. These shifts are listed as H in Table 1. For details of the kinematic coverage, please refer to Fig. 11, Fig. 12 and Fig. 13.

kin. P#	t, $(\mathrm{GeV}/c)^2$	θ_γ^{lab}, degree	θ_γ^{cm}, degree	θ_p^{lab}, degree	E_γ^{lab}, GeV	p_p, GeV/c	L, cm	H, cm
P1	-1.7	22	60	45	2.87	1.56	785	41.2
P2	-3.3	37	90	30	2.00	2.52	445	21.5
P3	-5.4	78	136	13	0.88	3.55	245	10.0

Table 1: The kinematics parameters of the proposed measurements at $s = 8$ $(\mathrm{GeV}/c)^2$.

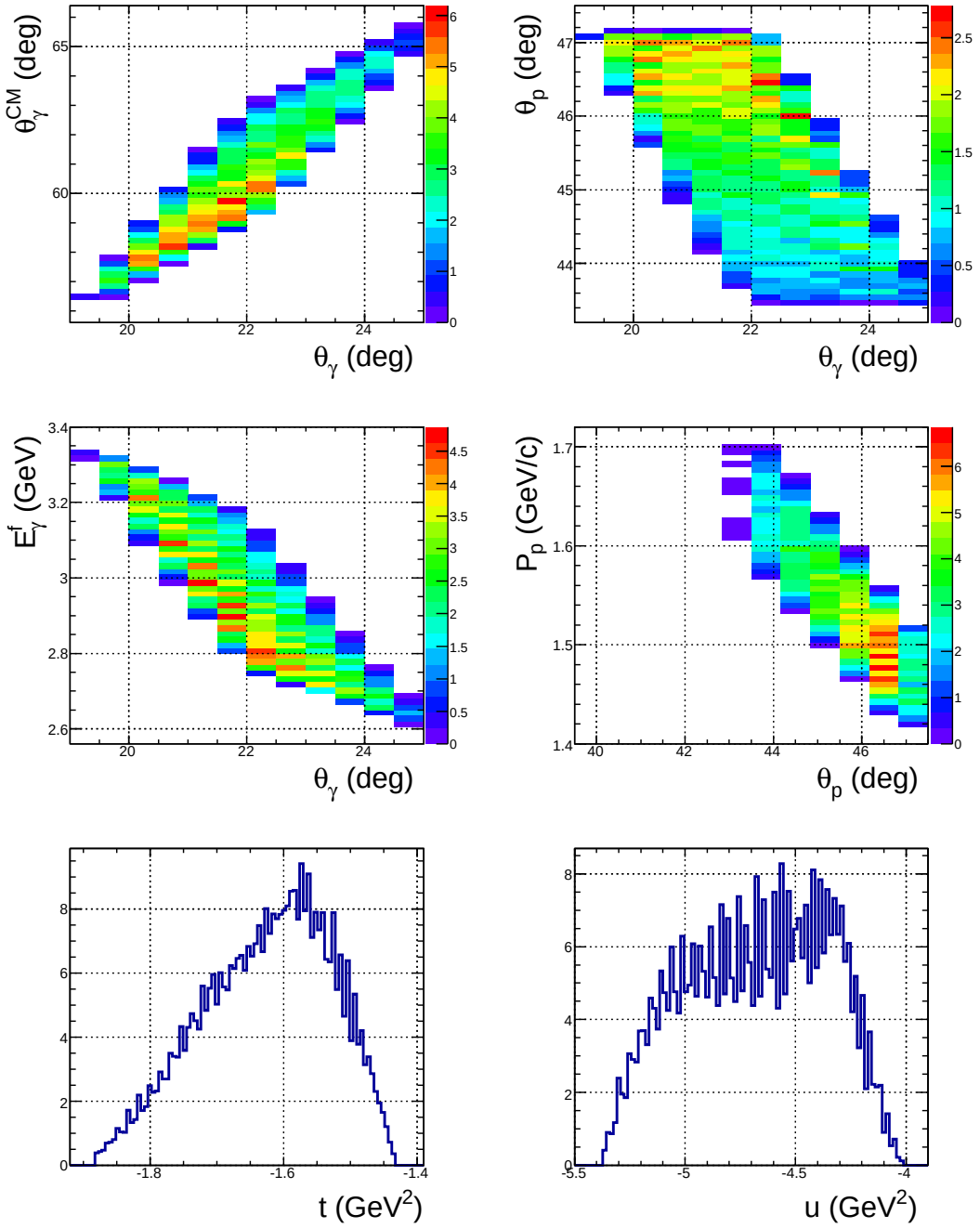

Figure 11: The kinematic coverage for $\theta^{cm} = 60°$ (P1) showing the angular (top) and momentum (middle) distributions for the detected photon (left) and proton (right). The θ_γ^{cm} is the center of mass angle for the photon, θ_γ is the lab angle for the photon, θ_p is the lab angle for the proton, E_γ^f is the photon energy, and P_p is the proton momentum. Also shown in the bottom plots are the mandelstam variables t (left) and u (right).

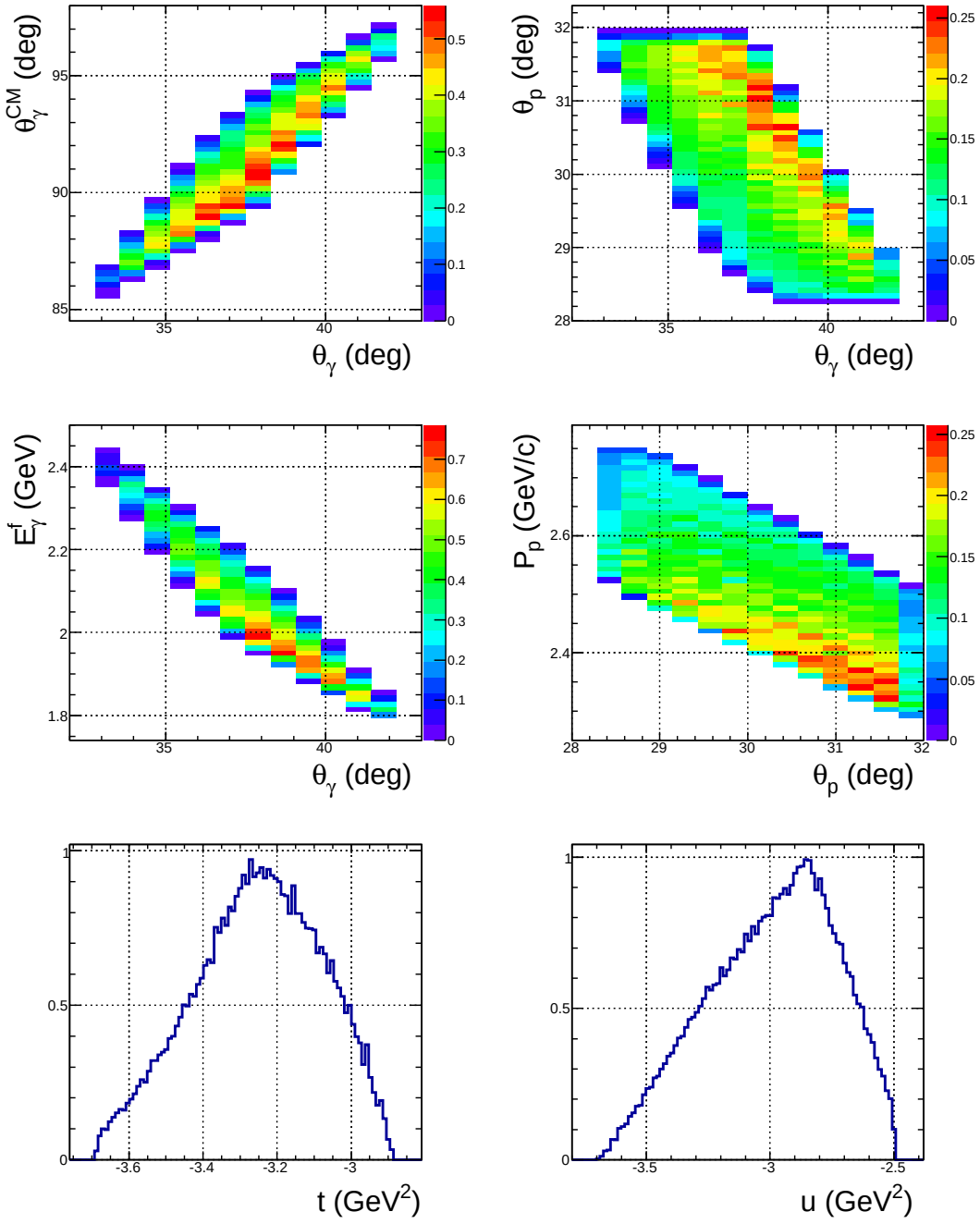

Figure 12: The kinematic coverage for $\theta^{cm} = 90°$ (P2) showing the angular (top) and momentum (bottom) distributions for the detected photon (left) and proton (right). The θ_γ^{cm} is the center of mass angle for the photon, θ_γ is the lab angle for the photon, θ_p is the lab angle for the proton, E_γ^f is the photon energy, and P_p is the proton momentum. Also shown in the bottom plots are the mandelstam variables t (left) and u (right).

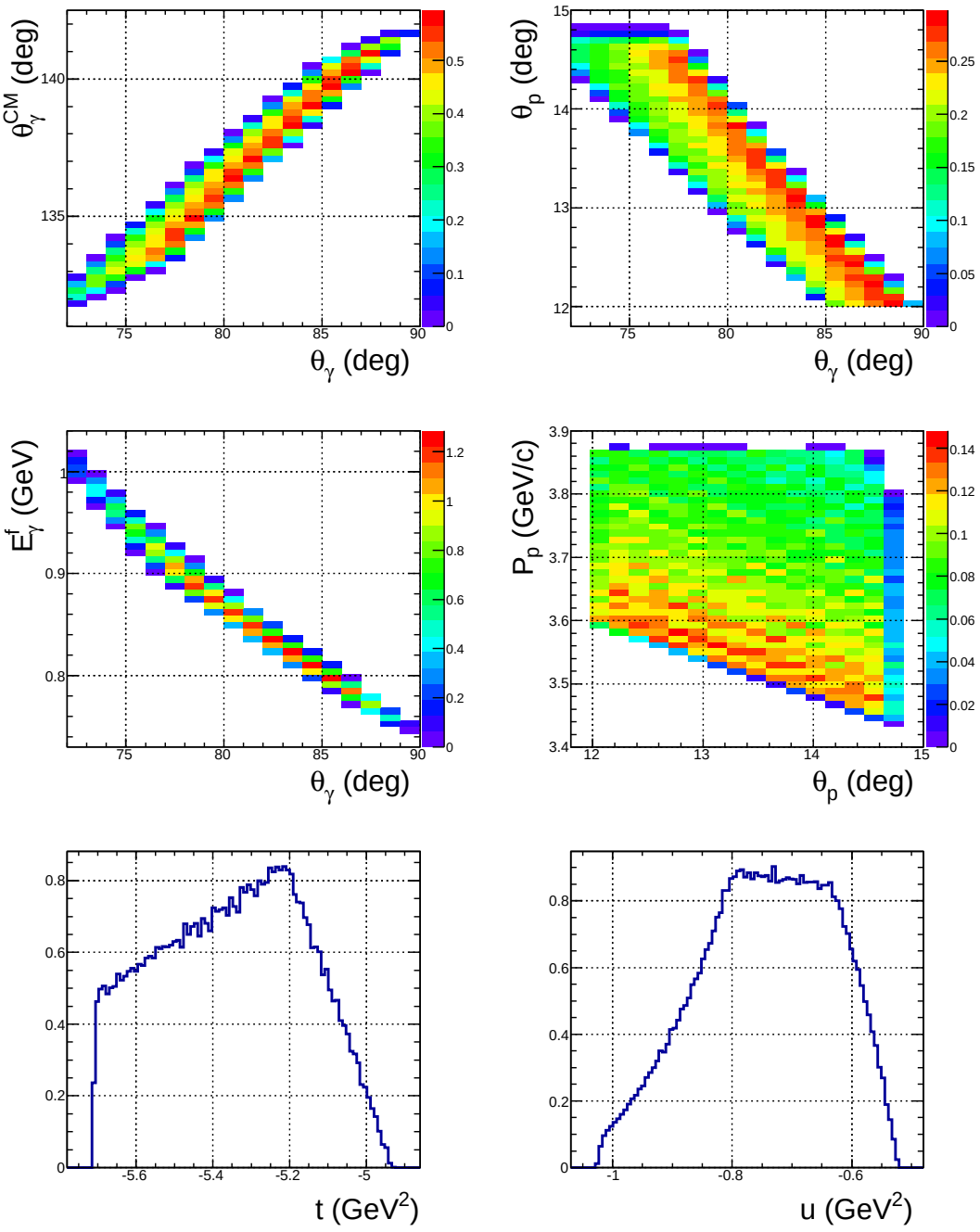

Figure 13: The kinematic coverage for $\theta^{cm} = 136°$ (P3) showing the angular (top) and momentum (bottom) distributions for the detected photon (left) and proton (right). The θ_γ^{cm} is the center of mass angle for the photon, θ_γ is the lab angle for the photon, θ_p is the lab angle for the proton, E_γ^f is the photon energy, and P_p is the proton momentum. Also shown in the bottom plots are the mandelstam variables t (left) and u (right).

4.2 Backgrounds

There are several sources of physics background in this measurement. The electrons, which lose energy while passing through the radiator and the target, can scatter elastically from the protons in the target. In this experiment the field of the polarized target magnet will provide sufficient deflection and we do not need to worry about them.

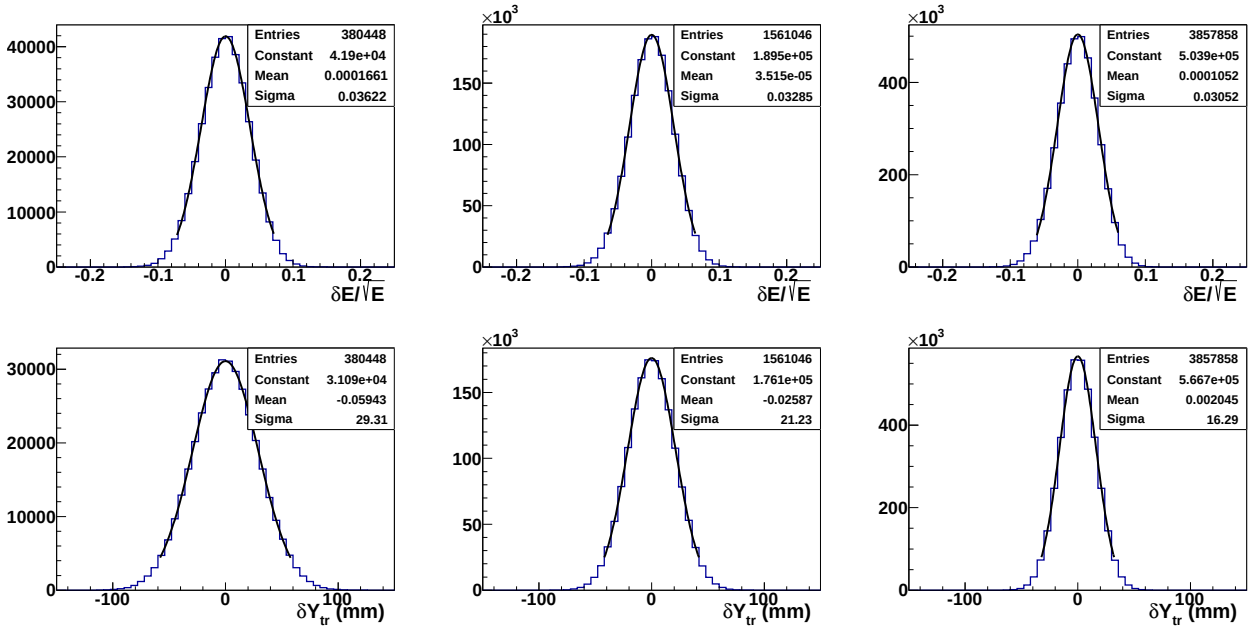

Figure 14: RCS correlation cuts of δE and δY for kinematics P1(left) and P2(center) and P3(right), where δE (top) is the difference between measured photon energy in the photon arm and the inferred photon energy, inferred by the measured proton in the proton arm, and δY(bottom) is the difference between measured photon horizontal position and the inferred photon horizontal position, in the transport frame. A gaussian fit (black curve) is also plotted on top of each histogram, with their fitted parameters labeled in the upper right corner in each panel. A 2σ cut will be used in the data analysis to select good RCS events.

Another source is the quasi-real photons from $ep\gamma$ event, $\mathrm{H}(e, p\gamma)e'$. Although the scattered electron is not detected, applying the $\gamma - p$ elastic kinematic correlation cuts, especially the δE, δY and δX cuts (see Fig. 14 for details) will remove most of them. δE is the difference between measured photon energy in the photon arm and the inferred photon energy, inferred by the measured proton in the proton arm. $\delta Y(X)$ is the difference between measured photon horizontal (vertical) position and the inferred photon horizontal (vertical) position, in the transport coordinate system. (The transport coordinate system is frequently used to define the acceptance and optics in small acceptance spectrometers like the HMS. In this

coordinate system, z axis is the central ray, which lines up with the spectrometer angle; x axis is vertically down and y axis is horizontally left when looking downstream.) According to our simulated result, $ep\gamma$ events drop rapidly as the scattering angle increases. The ratio of $ep\gamma$ events to RCS events under the 2σ cut is about 0.14, 0.08 and 0.03 for kinematics P1, P2 and P3, respectively. Our simulated $ep\gamma$ results match the existing E99-114 experiment pretty well, which states that the $ep\gamma$ contribution is about 11%-15% [46]. Nevertheless, these backgrounds can be analyzed and subtracted out in the data analysis.

The primary background comes from neutral pion photoproduction from the protons in the target. It can be separated only on a statistical level by using a difference in the shapes of the distribution of RCS and $H(\gamma, \pi^0)$ events. Fig. 15 shows the simulated δY and δX distribution, in the transport coordinate system, for the proposed kinematics. This background leads to a large dilution factor, which affects the statistical accuracy of the measurements. The pion can also be produced from bound protons in nitrogen. Motion of the nucleons in nuclei, and FSI, reduce dramatically the dilution of RCS events. The nuclear pion process was investigated by using E99-114 data obtained from an aluminum target. We found that at conditions similar to those proposed here, pions produced from nuclei increase the dilution factor by less than 10%.

4.3 Signal Extraction

It is not trivial to obtain data free of pion events. However, it is possible to obtain data free of RCS events, by selecting different regions of the δX and δY phase space, so that accurate numbers can be obtained for the asymmetry of pion events. It is then possible to measure the asymmetry for pure pion events, the asymmetry for mixed RCS-pion events, and the fraction of the latter events that are RCS. The latter number is just the inverse of the dilution factor D and is obtained by fitting spectra (shown in 19). Each step can contribute to the error in the resulting RCS asymmetry on both a systematic and statistical level. We now consider a technique of directly extracting the real Compton events negating the need for the asymmetry for mixed RCS-pion events.

To reduce uncertainty in the extracted real Compton events it is possible to use a boosted decision tree [41, 42, 43, 44] with multiple discriminating variables. A decision tree is a binary tree structure classifier which organizes the data into regions analyzing event by event. The decision tree algorithm is able to split the phase space into a large number of hypercubes, each of which is identified as either signal or background. The information entropy is used to optimize each split point. The boosting [45] performs best if applied to tree classifiers that, taken individually, have not much classification power. Using a small set of input variables with weak classification power still leads to a great reduction of uncertainty in the extracted counts.

As an example for separation of the RCS events from the pion background we use the discriminating variables δY, δX, and δP. The Monte Carlo is well tuned to the expected

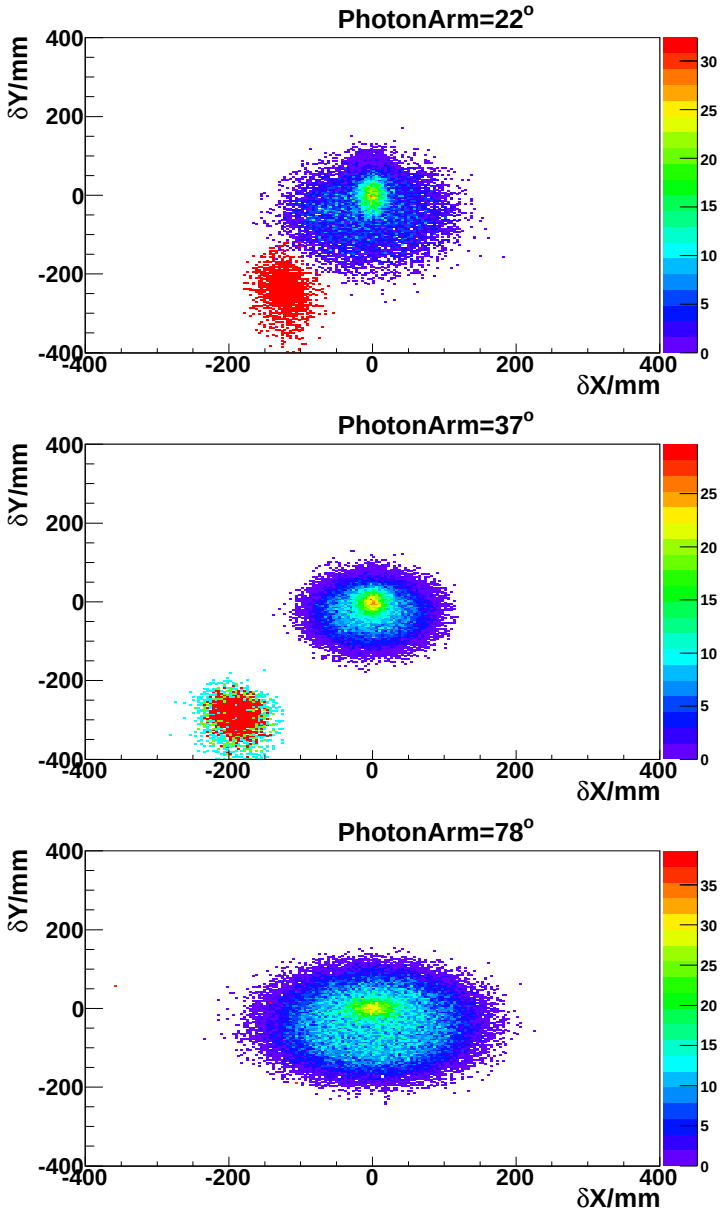

Figure 15: The δY and δX distribution, in the transport coordinate system, after applying δE cut for RCS events and backgrounds for kinematics P1(top), P2(middle) and P3(bottom). The RCS events are located at (0,0) and $e-p$ elastic events are deflected to negative δY and δX. The π^0 background is for the most part evenly distributed around the RCS signal. The statistics presented here correspond to the requested beam time.

resolution of the detection system so that reconstruction of these variables is expected to be within a realistic range in the simulation. The decision tree is then trained and classification using simulated data of signal and the neutral pion background is obtained.

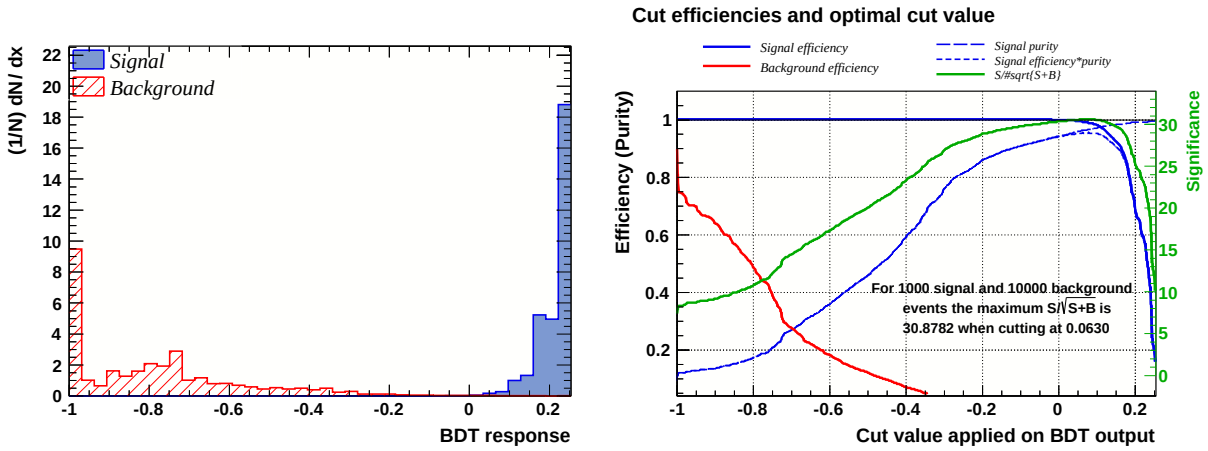

Figure 16: Results of analysis from the training of the boosted decision tree indicating (left) the response of the classifier and (right) the real Compton signal resolving efficiency.

Fig. 16 shows the boosted decision tree output. The result of analysis from the training of the boosted decision tree indicating the response of the classifier is shown in the left plot. The real Compton signal resolving efficiency as a function of the cut on the BDT response is shown in the right plot. Signal efficiency is show in blue and background efficiency is shown in red. The optimal cut is determined by using the derivative of the significance function $S/\sqrt{S+B}$ shown in green. The classifier response indicates that even with the only three mentioned discriminating variable it is possible to obtain greater then 98% signal when making a constraint on the BDT response to eliminate the pion background. The cut value applied on the BDT response is indicated on the right showing that only around 40 events from the pion background survive after the constraint is applied for a situation that started with an order of magnitude more π^0 background than the Compton signal. The separation using a Monte Carlo demonstration is shown in Fig. 17

This technique is especially useful for situations in which the background is difficult to distinguish from the signal in the spectra. Through the use of multivariate discrimination of the phase space even a small signal that is nearly unrecognizable among the background can be separated out with a well defined uncertainty associated with it. It the example illustrated the D value was reduced from 11 to 1.04. We do not propose the experiment with a reliance on this method but suggest it as a powerful complement.

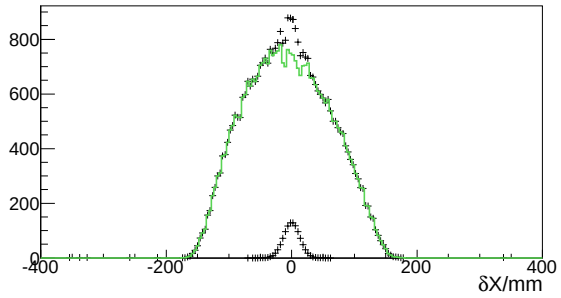

Figure 17: Here we show a δX distribution with signal and background before separation and after. The result of imposing the optimal BDT response cut at 0.063 leading to a RCS event extraction with 98% signal efficiency. This demonstrates a separation with 1000 Compton events with 10000 π^0 background events. This is only a Monte Carlo demonstration. All points that we propose have considerably less background.

4.4 Rates

The event rates are the products of the luminosity, the cross section, and the acceptances of the detectors, as well all other factors such as DAQ dead time and detection efficiency. The rate, N_{RCS} can be calculated as:

$$N_{RCS} = \frac{d\sigma}{dt}_{RCS} \frac{(E_\gamma^f)^2}{\pi} d\Omega_{\gamma p} A_{\gamma p} F_\gamma \mathcal{L}_{e\vec{p}}\,, \tag{10}$$

where $\frac{d\sigma}{dt}_{RCS}$ is the RCS cross section; the factor $\frac{(E_\gamma^f)^2}{\pi}$ is the Jacobian that converts dt to $dEd\Omega$; $d\Omega_{\gamma p}$ is the solid angle of the RCS events that expressed in photon detector; $A_{\gamma p}$ is the acceptance of RCS events in the given range of photon energy E_γ^f; F_γ is the number of photons per incident electron, $\mathcal{L}_{e\vec{p}} = 7.5 \cdot 10^{34}$ cm^{-2}Hz is the electron-proton polarized luminosity with the NH_3 target, including a correction for the extra heat load from the radiator.

E99-114 measured real compton scattering cross section at four electron beam energy of 2.342, 3.481, 4.620, and 5.759 GeV and θ_γ^{cm} in the range of $60^\circ - 130^\circ$. Table 2 shows their results for the average photon energy of 4.3 GeV. Also shown in the table is the dilution factor D, which is defined as the ratio of total γ seen from the π^0 and Compton signal to the γ seen from the Compton signal alone: $D = (N_{\gamma,\pi^\circ} + N_{\gamma,\gamma})/N_{\gamma,\gamma}$ for the kinematically correlated photon-proton events.

To estimate the RCS differential cross section, we adjusted J. Miller's model [40] to match the existing data from E99-114 [46]. Compared to E99-114 result, Miller's RCS differential cross section model has about 10% deviation from the 3.1 GeV data and 30% deviation form

kin. 4#	θ_γ^{lab}, degree	t, $(\mathrm{GeV}/c)^2$	θ_γ^{cm}, degree	D	$d\sigma/dt$, $\mathrm{pb}/(\mathrm{GeV}/c)^2$
4A	22	-2.03	63.6	2.13	496.
4B	26	-2.57	72.8	1.54	156.
4C	30	-3.09	81.1	1.67	72.
4D	35	-3.68	90.4	2.75	42.
4E	42	-4.39	101.5	2.80	29.
4F	50	-5.04	112.1	2.42	38.
4G	57	-5.48	119.9	2.83	46.
4H	66	-5.93	128.4	3.89	61.

Table 2: The RCS cross section at s = 9 $(\mathrm{GeV}/c)^2$- 4 pass kinematics in E99-114.

the 4.3 GeV data and 43% deviation form the 5.3 GeV data. We were able to scale the prediction and create a smooth curve to match the experimental data. An extrapolation of this curve was then used to estimate the cross section for our point P3. Miller's model has good constraints on the center of mass angle dependence and incident photon energy dependence. Therefore we used a 5th order polynomial function to scale Miller's model such that it matched the E99-114 data. For any given photon energy and θ_γ^{cm}, we can use a 2nd order interpolation to calculate the RCS differential cross section. With this modification we are able to estimate θ_γ^{cm} outside the range of E99-114. Fig. 18 shows the modified model together with E99-114 data points.

To determine the angular acceptance, we developed a Geant4 simulation program which included the target magnet coils, their magnetic field profile, and the geometry of NPS and the HMS. We placed the NPS and HMS at optimized locations and simulated RCS events, e-p elastic events and π^0 backgrounds. Finally we extracted the acceptance for RCS photons in a 3-D space of energy, θ, and ϕ. In the same way we determine the acceptance for electrons in the NPS and protons in the HMS.

For a 6% radiator, the photon flux can be calculated as:

$$F_\gamma = t_{rad}[\frac{4}{3}\ln(\frac{k_{max}}{k_{min}}) - \frac{4(k_{max}-k_{min})}{3E} + \frac{k_{max}^2 - k_{min}^2}{2E^2}]\,, \tag{11}$$

where k_{max} and k_{min} are the upper and lower limit of the radiated photon energies, E is the electron beam energy and t_{rad} is the thickness of the radiator in radiation lengths.

Our event rates are integrated over the 3-D space of energy, θ angle, and ϕ angle using Eq. 10. Table 3 shows the rates and dilution factors D. The expected δX distributions for RCS signal and backgrounds after applying the 2σ cuts to minimize the background (see Fig. 14), are presented in Fig. 19. The pure RCS signal is in red, with a gaussian fit (pink) on top of it. The fitted parameters are labeled in the upper right corner of each panel. The

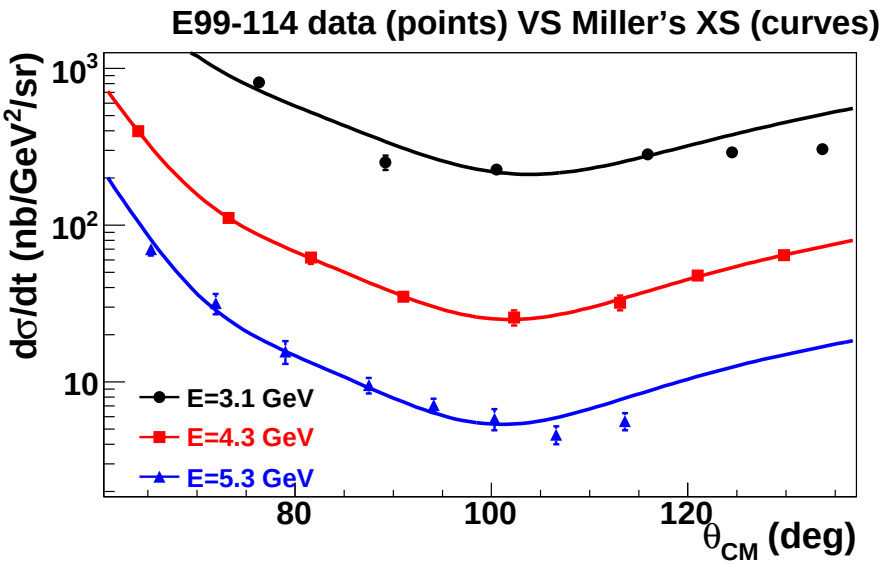

Figure 18: The RCS differential cross section. The solid curve is from modified Miller's model and solid points are the result from E99-114 [46].

e-p elastic events also shown in the figure but almost nothing survives after the 2σ δE and δY cuts. The statistics here represent 52, 293 and 185 hours of data taking for kinematics P1, P2 and P3, respectively.

kin. P#	θ_γ^{lab} degree	θ_γ^{cm} degree	RCS rate Hz	D	N_{RCS} per hour
P1	22	60	0.01254	2.0	45.1
P2	37	90	0.00158	2.8	5.7
P3	78	136	0.00211	3.9	7.6

Table 3: The kinematic parameters and the expected counts.

4.5 Required Statistics

The statistics required for obtaining the specified accuracy of ΔA_{LL} can be calculated from

$$N_{RCS,required} = D/(P_e P_p f_{e\gamma} \Delta A_{LL})^2$$

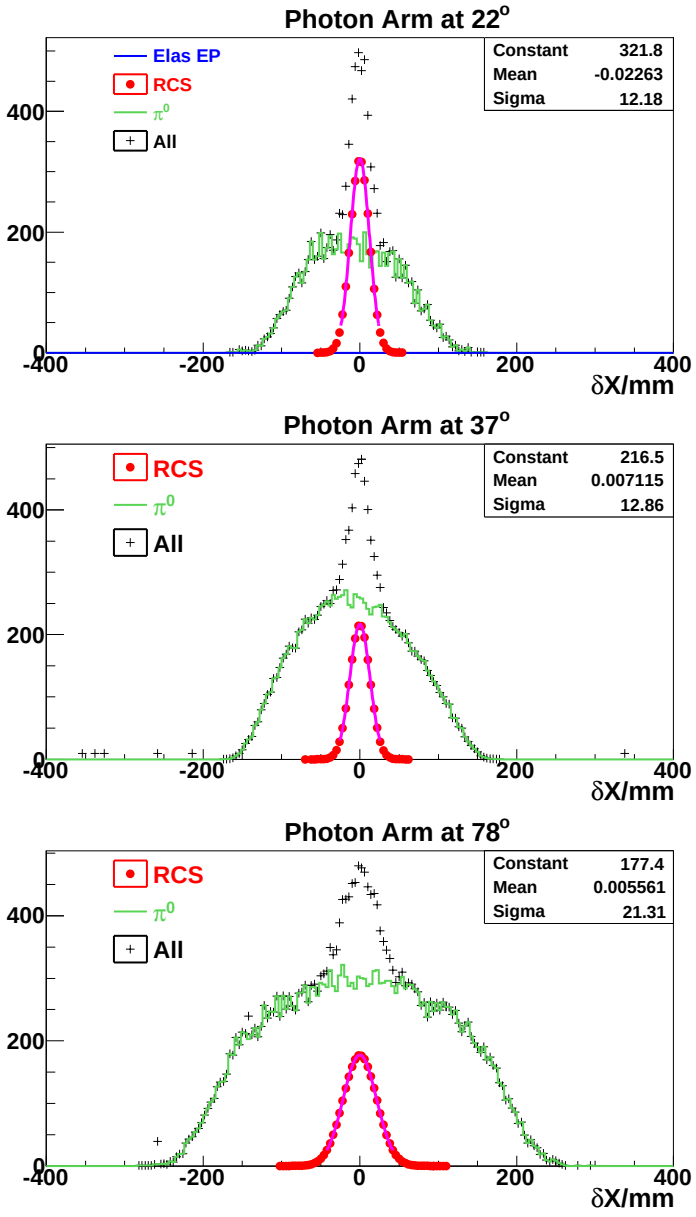

Figure 19: δX distributions after the δY cut, for kinematics P1(top), P2(middle) and P3(bottom). The pure RCS signal is red curves, with a gaussian fit (pink) on top of it. The fitted parameters are labeled in the upper right corner of each panel. The e-p elastic events also ploted in the figure but almost nothing survives after and δY cuts. The total (RCS+π^0) are the black curves. The δE cuts is also imposed on P1 to minimize the background in this picture.

where $P_e = 0.80$ is the electron beam polarization, $P_p = 0.75$ is the averaged proton polarization in the target, $f_{e\gamma} = 0.976$ is the ratio of the photon and the electron polarizations for the average $E_\gamma = 0.87E_e$. Table 4 presents the required statistics for a precision of better than $\Delta A_{LL} = 0.09$ for all kinematics points.

kinematic	P1	P2	P3
N_{RCS}, events	2333	1666	1404
ΔA_{LL}	0.05	0.07	0.09

Table 4: The statistics and expected precision in the proposed experiment.

4.6 Systematic Uncertainty

Source	Systematic
Polarimetry	5%
Packing fraction	3%
Trigger/Tracking efficiency	1.0%
Acceptance	0.5%
Charge Determination	1.0%
Detector resolution and efficiency	1.0%
Background subtraction	4.0%
Total	8%

Table 5: Estimates of the scale dependent contributions to the systematic error of A_{LL}.

Table 5 shows a list of the scale dependent uncertainties contributing to the systematic error in A_{LL}. With careful uncertainty minimization in polarization, the relative error in the target polarization can be less than or equal to 3.9%, as demonstrated in the recent E08-027/E08-007 experiment [47]. The polarized target uncertainty is combined with a 3% uncertainty in the beam polarization and obtain a total polarimetry uncertainty of about 5%. The uncertainty in the packing fraction of the ammonia target contributes at a level of less than 3%.

Charge calibration and detector efficiencies are expected to be known better to 1%. Detector resolution and efficiency is also expect to contribute less than 1%.

The signal extraction error will be minimized using a multivariate techniques leading to only a few counts of background slipping into the final result. The systematic error on resolving the Compton signal is dependent on the background produced at that kinematic

point. A larger background with smaller signal naturally results in a larger error. By considering a larger than expected background we can estimate the expected systematic error from a plausible analysis. Considering both π^0 and $ep\gamma$ background we expect less than a 4% background which is a estimate directly based on the Monte Carlo.

The primary sources of systematic error clearly come from polarimetry and background subtraction but the impact of time-dependent drifts in these quantities must be carefully controlled.

5 Expected Results and Beam Time Request

5.1 Expected Results

The purpose of this experiment is to measure the initial state helicity correlation asymmetry A_{LL} with a precision sufficient to obtain conclusive evidence on the dominance of the specific reaction mechanism. Another purpose is to determine the form factor ratio: R_A/R_V, which is also related to A_{LL}. We propose to obtain the statistical precision for A_{LL}, given in Table 4 and shown in Fig. 20. Using the handbag formalism to interpret the results of the A_{LL}, we will extract values for R_A/R_V.

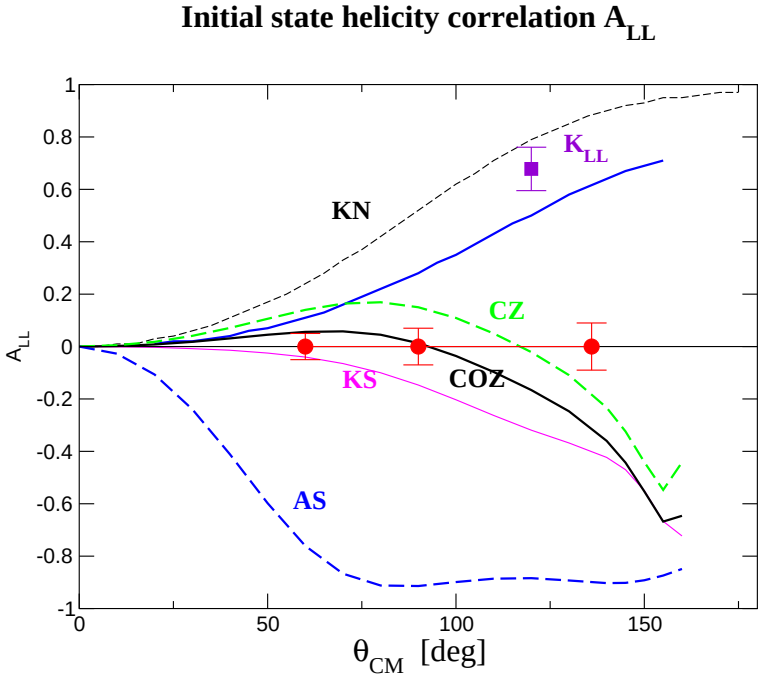

Figure 20: The initial state helicity correlation asymmetry A_{LL} in the RCS process with the expected precision of the proposed measurements shown as closed squares. The labels on the curves are as follows: CQM for the asymmetry in the constituent quark model[19]; the pQCD calculations[3] with AS for the asymptotic distribution amplitudes; with COZ for Chernyak-Ogloblin-Zhitnitsky [39]; GPD for calculations in the soft overlap approach[11]. The K_{LL} result[8] from E99-114 is also shown.

5.2 Beam Time Request

The proposed experiment is done at one beam energy of 4.4 GeV with currents of 90 nA. The requested beam time summarized in Table 6.

We require 8 hours to calibrate the calorimeter with $e - p$ elastic coincident events. The radiator will be out of the beam line during this procedure. To measure the packing fraction of the material in the target cell, we need 22 hours in total to do a empty cell and carbon target measurements. We need to measure the beam polarization with the Möller polarimetry every time the beam conditions change. We estimate the frequency to be on the order of once every other day. It will take about 3 hours for each measurement. In total we requested 33 hours.

Also shown in Table 6 is a summary of the time required for configuration changes. It will take less than 3 hours to perform each anneal of the target in order to restore the optimal target polarization. We will need an anneal every 1 to 2 days based on the latest experience in E08-007 and E08-027. In the worst case, we might need to remove the target stick 3 times to insert fresh material. These changes should take less than 15 hours total to change the material. We estimate 25 hours committed to target polarization calibrations. To change kinematics (move NPS and HMS), it will require about 3 hours for each change. We estimate 133 hours of overhead. The total time requested is a combination of the required beam time and the overhead time. The total request is 742 hours, or 31 days.

Kin. P#	Procedure	beam, nA	time hours
P1	RCS data taking	90	52
P2	RCS data taking	90	293
P3	RCS data taking	90	185
P1	NPS and HMS calibration	1000	8
P2	NPS and HMS calibration	1000	8
P3	NPS and HMS calibration	1000	8
	Packing Fraction	90	22
	Moller Measurements	200	33
	Beam Time		609
	Target Anneals		55
	Target T.E.		25
	Stick Changes		15
	BCM calibration		13
	Optics		13
	kinematics change		12
	Total Requested Time		742

Table 6: The beam time request for the experiment.

6 Technical Considerations

There is already a polarized target experiment approved for Hall C (E12-13-011) which will using the same target infrastructure and HMS.

With proper planning the transition from one experiment to the next would require a reconfiguration of the target and detector system. With proper planning the transition from one experiment to the next would be short in duration and only require tuning the HMS for protons and moving the NPS and the HMS into position.

The radiator will have to be able to move in and out within the scattering chamber. It will be mounted such that it can be moved into and out of the beam as necessary so that it would not interfere with the other experiment. The experiment requires support from JLab. In addition to the installation of the polarized target we will also require beam line instrumentation workable at the proposed beam current. In addition we need the large, slow raster that distributes the beam uniformly on the surface of the target.

7 The Collaboration

This collaboration consists of members with extensive experience using the UVA polarized target in Hall C. In addition, the collaboration includes many individuals from the RCS collaboration and the NPS collaboration with experience in electromagnetic calorimetry. The JLab target group together with the UVA target group will handle installation, calibration and operation of the polarized target.

8 Summary

We request 742 hours of beam time to measure the initial state helicity correlation asymmetry A_{LL} in RCS at s= 8 (GeV/c)^2 for $\theta_\gamma^{cm} = 60^\circ$, 90° and 136° with statistical uncertainty of 0.05, 0.07 and 0.09, respectively. This experiment will take place in Hall C, utilizing a 4.4 GeV, 90 nA and 80% polarized electron beam, plus the UVA/JLAB polarized target (longitudinally polarized), and HMS to detect protons, and NPS to detect scattered photons. This is a unique opportunity to study the initial state polarization effects in RCS.

Knowledge of the initial state helicity correlation asymmetry A_{LL} in RCS at these kinematics will allow a rigorous test of the reaction mechanism for exclusive reactions at high t, which is crucial for the understanding of nucleon structure.

Furthermore, it will be an extended measurement of the proton axial form factor R_A in RCS, which is the $1/x$ moment of the polarized parton distribution.

References

[1] S. J. Brodsky and G. Farrar, *Phys. Rev. Lett.* **31**, 1153 (1973).

[2] V. A. Matveev, R. M. Muradyan, and A. V. Tavkheldize, *Lett. Nuovo Cimento* **7**, 719 (1973).

[3] T. Brooks and L. Dixon, *Phys. Rev.* **D 62** 114021 (2000)

[4] C. Bourrely, J. Soffer, Eur. Phys. J. **C 36** 371 (2004)

[5] M. Jones *et al.*, *Phys. Rev. Lett.* **84**, 1398 (2000).

[6] O. Gayou *et al.*, *Phys. Rev. Lett.* **88**, 092301 (2002).

[7] A. Puckett *et al.*, *Phys. Rev. Lett.* **104**, 242301 (2010).

[8] D. J. Hamilton *et al.* [Jefferson Lab Hall A Collaboration], arXiv:nucl-ex/0410001.

[9] A.V. Radyushkin, *Phys. Rev.* **D 58**, 114008 (1998).

[10] M. Diehl, T. Feldmann, R. Jakob, P. Kroll, *Eur. Phys. J.* **C 8**, 409 (1999).

[11] H. W. Huang, P. Kroll, T. Morii, *Eur. Phys. J.* **C 23**, 301 (2002), *Erratum ibid.*, **C 31**, 279 (2003); H. W. Huang, private communication.

[12] F. Cano and J. M. Laget, Phys. Lett.**B 551** (2003); Erratum-ibid.**B 571**:260, (2003).

[13] X. Ji, *Phys. Rev.* **D 55**, 7114 (1997), *Phys. Rev. Lett.* **78**, 610 (1997).

[14] A.V. Radyushkin, *Phys. Lett.* **B 380**, 417 (1996),

[15] N. Kivel and M. Vanderhaeghen, JHEP 1304 (2013) 029; arXiv:1212.0683.

[16] N. Kivel and M. Vanderhaeghen, arXiv:1312.5456 [hep-ph].

[17] G. Eichmann and C. S. Fischer, *Phys. Rev.* **D 87**, 036006 (2013).

[18] M. Diehl, P. Kroll, *Eur. Phys. J.* **C 73**, 2397 (2013), arXiv:1302.4604.

[19] G. A. Miller, *Phys. Rev.* **C 69**, 052201(R) (2004).

[20] A. Nathan, R. Gilman and B. Wojtsekhowski, spokespersons, JLab experiment E07-002.

[21] G. P. Lepage and S. J. Brodsky, *Phys. Rev.* **D 22**, 2157 (1980).

[22] A. Radyushkin, arXive:hep-ph/0410276 and Dubna preprint JINR P2 10717.

[23] G. R. Farrar and H. Zhang, *Phys. Rev. Lett.* **65**, 1721 (1990), *Phys. Rev.* **D 42**, 3348 (1990).

[24] A. S. Kronfeld and B. Nizic, *Phys. Rev.* **D 44**, 3445 (1991); M. Vanderhaeghen, P. A. M. Guichon and J. Van de Wiele, *Nucl. Phys.* **A 622**, 144c (1997).

[25] K. Wijesooriya *et al.*, *Phys. Rev. C***66**, 034614 (2002).

[26] M. Diehl, T. Feldmann, R. Jakob and P. Kroll, *Eur. Phys. J.* **C 39**, 1 (2005) arXiv:hep-ph/0408173.

[27] G. A. Miller, *Phys. Rev.* **C 66**, 032201 (2002).

[28] M. Diehl, T. Feldmann, H. W. Huang and P. Kroll, Phys. Rev. D **67**, 037502 (2003) [arXiv:hep-ph/0212138].

[29] E. Lomon, *Phys. Rev.* **C 66**, 045501 (2002).

[30] R. L. Anderson *et al.*, *Phys. Rev.* **D 14**, 679 (1976).

[31] M. Battaglieri *et al.*, *Phys. Rev. Lett.* **87**, 172002 (2001).

[32] T. H. Bauer *et al.*, Rev. Mod. Phys. **50**, 261 (1978).

[33] M. A. Shupe *et al.*, *Phys. Rev.* **D 19**, 1921 (1979).

[34] C. Perdrisat *et al.*, JLab experiment E01-109, 2001.

[35] N. Dombey, Rev. Mod. Phys. 41, 236 (1969).

[36] N. Dombey, Rev. Mod. Phys. 41, 236 (1969).

[37] T. W. Donnelly and A. S. Raskin, Ann. Phys. (New York) 169, 247 (1986); 191, 81 (1989).

[38] Spin Asymmetries of the Nucleon Experiment, JLAB E-03-109, O.Rondon, Z.E. Meziani, and S. Choi, spokespersons.

[39] V. L. Chernyak A. A. Oglobin, and A. R. Zhitnitsky, *Z. Phys.* **C 42**, 569 (1989).

[40] G. Miller, Phys. Rev. C, 69, 052201.

[41] L. Breiman, J. Friedman, R. Olshen and C. Stone, "Classication and Regression Trees", Wadsworth International Group, Belmont, California (1984).

[42] J. Friedman, T. Hastie, and R. Tibshirani, "Additive logistic regression: a statistical view of boosting", Annals of Statistics 28 (2), 337-407 (2000).

[43] Y. Freund and R.E. Schapire, A short introduction to boosting, Journal of Japanese Society for Artificial Intelligence, 14(5), 771-780.

[44] J. Friedman, Recent Advances in Predictive (Machine) Learning, Proceedings of Phystat2003, Stanford University, (September 2003).

[45] R.E. Schapire, The boosting approach to machine learning: An overview, MSRI Workshop on Nonlinear Estimation and Classification, (2002).

[46] A. Danagoulian *et al.*, Phys. Rev. Lett, 98, 152001 (2007).

[47] D. Keller, Nucl. Inst. and Meth. A 728 133-144 (2013)

Appendix

A Hall C Neutral Particle Spectrometer (NPS)

Neutral Particle Spectrometer (NPS) Facility in Hall C

Update to Jefferson Lab PAC 42

June 1, 2014

A. Camsonne, R. Ent, P. Nadel-Turoński, S.A. Wood, B. Wojtsekhowski, C. Zorn
Jefferson Lab, Newport News, VA 23606

A. Asaturyan, A. Mkrtchyan, H. Mkrtchyan, V. Tadevosyan,
S. Zhamkochyan
A.I. Alikhanyan National Science Laboratory, Yerevan 0036, Armenia

M. Guidal, C. Munoz Camacho, R. Paremuzyan
Institut de Physique Nucleaire d'Orsay, IN2P3, BP 1, 91406 Orsay, France

I. Albayrak, M. Carmignotto, N. Hlavin, T. Horn[1]
F. Klein, B. Nepal, I. Sapkota
The Catholic University of America, Washington, DC 20064

C. Hyde, M.N.H. Rashad
Old Dominion University, Norfolk, Virginia

P. King, J. Roche
Ohio University, Athens, OH 45701

D. Day, D. Keller, O. Rondon
University of Virginia, Charlottesville, VA, USA

D.J. Hamilton, J.R.M. Annand
University of Glasgow, Glasgow, Scotland, UK

S. Sirca
University of Ljubljana, Ljubljana, Slovenia

D. Dutta
Mississippi State University

[1] Contact person: hornt@jlab.org

Contents

I. INTRODUCTION

The Neutral Particle Spectrometer (NPS) is envisioned as a facility utilizing the well-understood HMS and the infrastructure of the SHMS to allow for precision (coincidence) cross section measurements of neutral particles. It can be canelevered off the SHMS carriage covering detection angles between 5.5 and 30 degrees, and be positioned on top of the SHMS carriage to cover angles between 25 and 60 degrees. The NPS will be used as photon detector for an approved Deeply-Virtual Compton Scattering [1] experiment, E12-13-010, that aims to extract the real part of the Compton form factors without assumptions. It will also be used as neutral-pion detector for π° electroproduction in semi-inclusive Deep-Inelastic Scattering, in approved experiment E12-13-007, to validate our basic understanding of the partonic interpretation of these reactions with several experimental advantages as compared to likewise charged-pion reactions [2]. Here, the neutral pion will be detected by measurement of its $\gamma\gamma$ decay products.

The NPS could further be used as photon detector for Wide-Angle Compton Scattering [3, 4] reactions, and as neutral-pion detector for exclusive π° photoproduction [5], proposals submitted to this PAC.

The basic concept for the NPS is a highly segmented electromagnetic calorimeter preceded by a compact sweeping magnet. The experiments it enables require detection of neutral particles with energies ranging between ≈ 1 and ≈ 8 GeV, with good energy resolution (1-2%), and good coordinate (2-3 mm) and angular (0.5-1 mr) resolution, comparable to the resolutions of the focusing spectrometers in Hall C. The neutral particle scattering angles cover 6.7-25 degrees for the approved program, and up to 60 degress for the foreseen program. The distance of the calorimeter from the target ranges from 3 to 12 meters. As an example, the minimum angle of the approved program at a distance of 4 m is 7.2°.

The NPS is an efficient and economical way to meet all of the presently known experimental requirements. It will consist of the following components:

- $PbWO_4$ crystals in a temperature controlled frame;
- a set of high voltage distribution bases with built-in amplifiers [6] for operation in high-rate environments;
- essentially deadtime-less digitizing electronics to independently record the pulse amplitudes from each crystal;
- a sweeping magnet of roughly 0.3-0.6 Tm;
- a cantelevered platform of the SHMS carriage to allow precise, remote rotation around the Hall C pivot over an angular range between 5.5 and 30 degrees;
- a platform to mount the NPS on top of the SHMS carriage to allow precise, remote rotation around the Hall C pivot over an angular range between 25 and 60 degrees;
- a light monitoring and curing system to monitor and restore crystal optical properties.

A more detailed description of the NPS facility is in a document submitted to PAC40 [7]. In this update document we will highlight present planning, and progress and results from some of our studies on the critical components of the calorimeter, leading towards a small prototype. We will present some of the results from our studies on LEDs used for gain monitoring and possible curing, phototube sensitivity to infrared light, plans for crystal irradiation and curing tests, as well as details and progress of assembly of the prototype and its LED curing system.

II. NPS CALORIMETER

The NPS calorimeter will consist of an array of up to 1116 scintillating $PbWO_4$ and up to 208 PbF_2 crystals, covering a solid angle of 25 msr at a distance of 4 m from the target. In general, the NPS requires

crystals with high transparency, high light yield, good timing where 90% of the light is emitted within 30-50 ns, and good radiation hardness. Also important are crystal geometry and integrity.

In the ideal case, the NPS calorimeter will consist of a set of brand new $PbWO_4$ crystals. Taking advantage of the existing $PbWO_4$ crystals (and accompanying photomultiplier tubes (PMTs)) of the high-resolution inner part of the Hybrid Electromagnetic Calorimeter (HYCAL) [8] used for the PrimEx/PrimEx-II experiments, one arrangement is an assembly of 1080 $PbWO_4$ crystals in a 36 by 30 matrix. Our goal is to acquire new $PbWO_4$ crystals, both to allow flexibility of scheduling of experiments at Jefferson Lab (given that more and more experiments plan to use $PbWO_4$ crystals) and to increase radiation hardness. Nonetheless, given the worrying lack of qualified vendors of $PbWO_4$ crystals in the world, and to evade scheduling conflicts, we investigate an alternate arrangement consisting of $\approx$ 600 $PbWO_4$ crystals and the available 208 PbF_2 crystals from the Hall A DVCS calorimeter, to complete a calorimeter with similar solid angle. The 600 $PbWO_4$ and $\approx$200 PbF_2 crystals would provide a hybrid calorimeter configuration. A similar but not identical hybrid calorimeter was succesfully used in the PrimEx HYCAL calorimeter, which had an inner core of $PbWO_4$ and an outer ring of lead glass crystals.

A. Choice of Crystals

Analysis of general properties of heavy crystals used in calorimetry show that BGO, $PbWO_4$, PbF_2 and LSO/LYSO are among the candidates. BGO is a commonly used scintillation crystal with a timing property of 300 ns, and is not suitable for the NPS calorimeter. LSO/LYSO crystals have acceptable timing properties, but do not provide an economically favorable option as they would be prohibitively expensive for our envisioned sizes.

Both $PbWO_4$ and PbF_2 crystals are fast, 5-14 ns for $PbWO_4$ and $<$30 ns for PbF_2, and are suitable for experiments requiring fast signals with short tails to minimize pile-up at high rates. This choice is of course also dictated by availability of these type of crystals used in JLab DVCS and PrimEx experiments.

Since the NPS calorimeter may by necessity perhaps be a combination of $\sim$600 $PbWO_4$ blocks (from PrimEx) and 208 PbF_2 blocks (from Hall A DVCS), the component studies should be optimized to include this possibility. This includes taking into account that for $PbWO_4$ crystals the mechanism of light emission is pre-dominantly scintillation, while it is pure Cherenkov radiation for PbF_2. The difference in dimensions and optical properties of $PbWO_4$ and PbF_2 crystals may similarly require different intensity for light monitoring.

B. Crystal Transmittance Measurements

One obvious question that needs addressing for a hybrid calorimeter is if we could use a single primary light source for both $PbWO_4$ and PbF_2 crystals. Hence, we first have to know the transmittance of light for both types of crystals.

We measured the transmittance of $PbWO_4$ and PbF_2 crystals using an existing setup of Jefferson Lab's Radiation Detector and Imaging group, in the ARC. The results are shown in Fig. 1. Comparison of the transmittance curves illustrates that $PbWO_4$ and PbF_2 crystals are very similar in the region above λ $\sim$400 nm, even if different in the short wavelength region (λ $\sim$250-350 nm). Hence, for instance blue light with a wavelength $\sim$470 nm should be acceptable for both types of crystals as a common light source for a monitoring system.

Note that the output pulse timing and shape for the crystals will be different. It would be preferable to use the same digital filtering for actual physics events and light pulser events, but if this difference is significant it may require a different digital filtering.

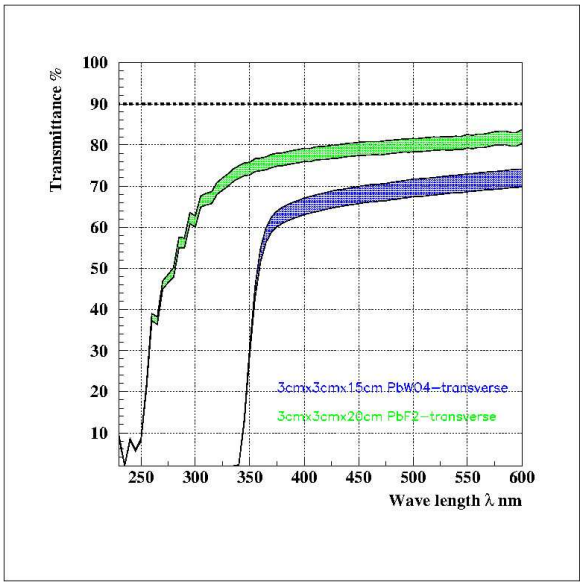

FIG. 1: *Light Transmission efficiencies of the PbF_2 (green) and $PbWO_4$ (blue) crystals (3.0 cm thickness) versus light wave length. Color bands represent spread in data measured at different points of the crystals.*

III. CURING SYSTEM AND COMPONENT STUDIES

All known crystals suffer from radiation damage. The most common damage phenomenon is radiation-induced absorption (reduction in crystals light attenuation length). Previous studies show that the $PbWO_4$ crystal scintillation mechanism is not damaged up to a radiation dose of 2.2 Mrad. Radiation damage of the crystals themselves show a clear saturation, and both transmittance and light yield are stabilized after an initial dosage of a few tens to 50-100 krad, with the level of damage at saturation being dose dependent. Naturally, the radiation damage will depend on the chemical composition of the crystals, and the type and amount of the dope material.

Studies of the radiation conditions in Hall C show that during the planned experiments the accumulated radiation dose may well exceed 100-200 krad, especially for small-angle operation of NPS. To keep the calorimeter performance at the required precision level of understanding efficiency and resolution, we plan to develop a light curing system, and periodically use this between different kinematic settings of the experiments, or whenever the accumulated dose will reach ∼50 krad.

A. General Concepts of Curing System

To restore the crystal optical properties, a curing system will be developed with as minimum impact on the running of the experiments. Our baseline method is to use blue light of wave length between 400 and 500 nm for so-called optical bleaching. It is well established that blue light is most effective in removing the radiation damage and resetting the crystal's attenuation length. The required light intensity is of an order of 1-2 mW/cm^2, and thus for the NPS 20×20 mm^2 ($PbWO_4$) or 30×30 mm^2 (PbF_2) crystals we need a curing system with power of 5-10 mW/crystal. Standard curing with blue light can be very effective: nearly 90% of the original signal can be restored within first 200 minutes with a photon flux of $\sim 10^{16}$ γ/s. However, the technique is invasive (requiring turning PMTs off and Hall access), and based on experience with the Hall A/DVCS experiment can affect PMT operation.

Thus, we also plan to study a curing system with permanent infrared illumination based on those from, *e.g.*, Refs. [9, 10]. Studies show that at such longer wavelengths (600-1000 nm) a significant recovery is possible,

but for a long time of irradiation. This is proven to work very well for low doses (∼3 krad) and can be operated remotely without access to the experimental area. The main difficulty of this method is the lower efficiency, by a factor of 20-50 relative to blue light, which then must be compensated by an increase of the light intensity (up to $\sim 10^{16}$ photons/s per block).

We plan to design, build and test both systems, based on blue and on permanently installed super bright infrared light ($\lambda \geq$940 nm). To be compatible with the NPS, they will have similar mechanical design. For both the curing and the light monitoring systems, detailed studies and selection of the most effective Light Emitting Diodes is critical.

B. Selection of Blue and Infrared LEDs

It is important to select LEDs that can withstand ∼1 Mrad or higher radiation doses without significant degradation (radiation hard LEDs). This strongly depends on the material used in LED production. The best radiation hardness are shown by LEDs based on SiC, GaN and AlGaInP (see [12, 13] and references there). Radiation hardness of the LEDs has been tested with protons, neutrons and photons. It was shown that for GaAs-based LEDs the normalized light output drops by factor ∼5 after radiation doses of 5×10^8 - 10^{10} p/cm^2 caused by protons or neutrons, the degradation effect from photons is 100-1000 times lower: for an accumulated dose of ∼1 kGy (∼100 krad) from photons no noticeable change in the light output or timing characteristics of GaAs-based LEDs was observed.

1. Infrared LED Studies

We have used a test setup of the Radiation Detector and Imaging Group to measure the absolute intensity of several types of blue (RL5-5515, RL5-4630 and SLA-580BCT3F) and infrared (NIR LD-274-3 and TSAL7400) LEDs. Some details of the setup are shown in Fig. 2. The infrared LED (seen on the left) is mounted on a special support structure. The calibrated Photodiode S2281 (seen on right) with an effective area of 100 mm^2 and quantum efficiency of ∼ 67% (at λ ∼950 nm) measures intensity of the emitted light (its current is nearly linearly proportional to the LED intensity). The distance between LED and Photodiode can be varied from 0.5 cm to 20 cm. The LED driving current is measured by a FLUKE multimeter and the Photodiode current is measured by high accuracy KEITHLEY picoamperemeter.

All equipment is installed in a *mini-dark-room*. With closed doors the photodiode dark current, with LED OFF was on the level of ∼0.001 nA. With the doors open the dark current value jumped to 1.1 μA (about 1000 times higher). Though all the LED studies were done with closed doors, this value of dark current is so small that one could do measurements with the doors open.

The electronic circuit which drives the LED used a fixed 5.0 V of the power supply. The value of the LED driving current was then changed over the range from 0 to 100 mA by changing the value of a 1 kΩ variable resistor. We then measured the LED emission intensity versus this driving current with the photodiode located at distances of both ∼3 cm and ∼7 cm from the LED. Results for both infrared LEDs are shown in Fig. 3. At a distance of ∼3 cm, where the LD-274-3 LED fully illuminates the calibrated photodiode (with an effective area of 100.0 mm^2) the energy output is equivalent to 2×10^{16} $\gamma/sec/cm^2$.

The wavelength of the LD-274-3 LED is λ=950 nm at the peak intensity. Using this number as an average to estimate energy of the photons, one obtains an equivalent energy of 1.3 eV:

$$E_\gamma = h \times \nu = h \times c/\lambda = (6.63^{-34}\ m^2kg/s \times 3 \times 10^8\ m/s)/(950 \times 10^{-9}\ m) \approx 1.31\ eV. \quad (1)$$

A photon flux $N_\gamma = 2 \times 10^{16}\gamma/s$ will then deposit a power of $P_\gamma = N_\gamma \times E_\gamma = 2 \times 10^{16} \times 1.31\ eV/s \approx 4.2\ mW$ per cm^2 (at a mean wavelength of 950 nm and at a nominal maximum current of 100 mA driving the LED, as listed in the Osram data sheet).

The data show that the emission intensity is almost linear with driving current. Beyond 60 mA, the output begins to curve slightly indicating the onset of saturation of the emission intensity of the LED. We verified that

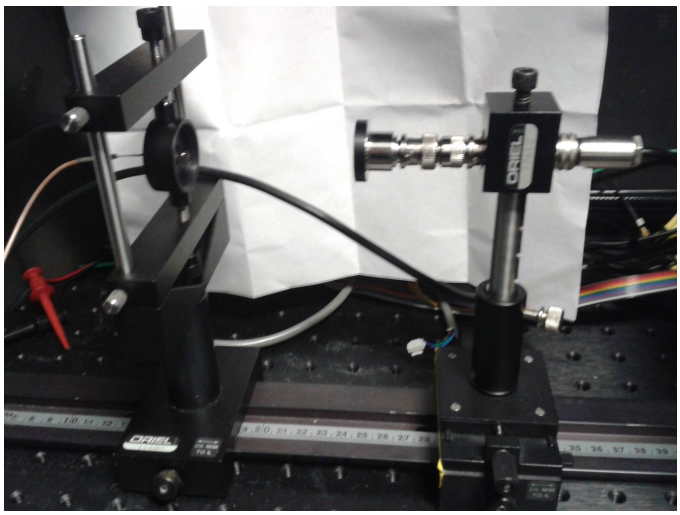

FIG. 2: *LED test setup. An infrared LED (on the left) is mounted on a special support structure. The calibrated Photodiode S2281 (on the right) with an effective area of 100 mm^2 measures the intensity of the emitted light. The distance between LED and Photodiode can be varied from 0.5 cm to 20 cm.*

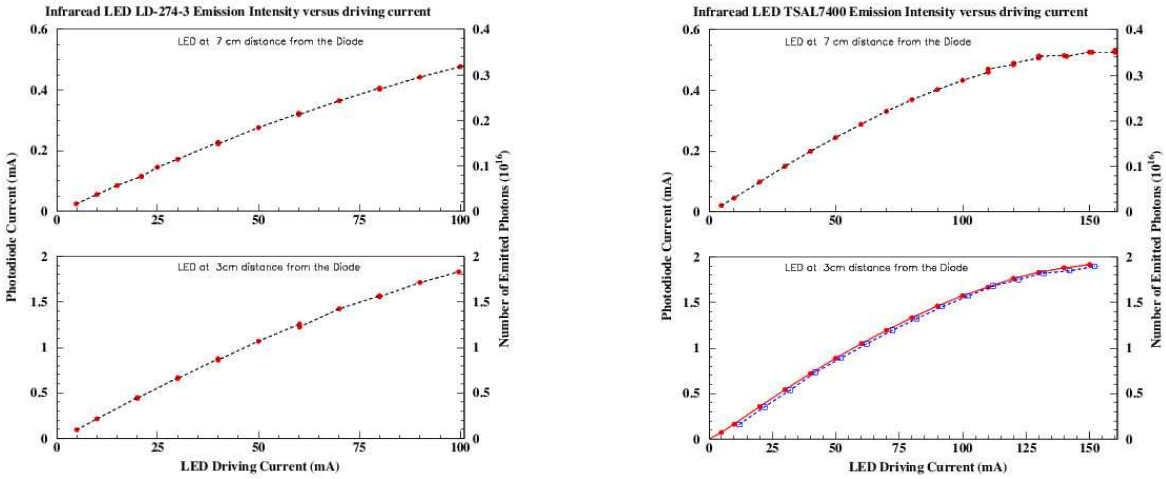

FIG. 3: *Emission intensity of the Infrared LED LD-274-3 (left) and TSAL7400 (right) versus driving current at distance 7 cm (top) and 3 cm (bottom).*

this saturation is due to the LED and not the photodiode by doing additional measurements with attenuation of the LED light output, by installing neutral density filter with attenuation factor of 9.25 in front of the LED. The data without filter and with filter, when scaled by the attenuation factor, are in good agreement.

2. Blue LED studies

The same experimental setup and the same technique were also used to study the emission intensity of several types of blue LEDs, as a function of both the driving current and the distance from the photodiode. Data for a distance of ∼3 cm are shown in Figs. 4 and 5.

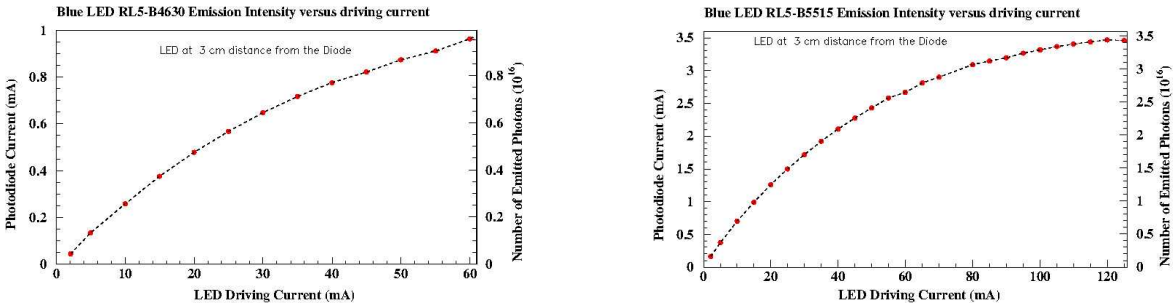

FIG. 4: *Emission intensity of the Blue LED RL5-B4630 (left) and RL5-B5515 (right) versus driving current at a distance of 3 cm.*

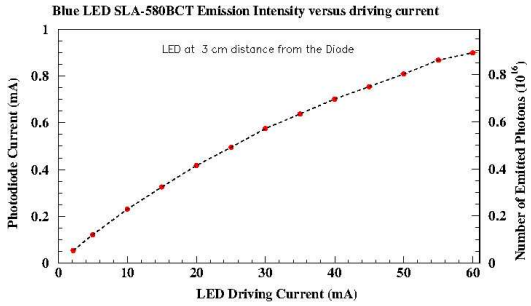

FIG. 5: *Emission intensity of the Blue LED SLA-580BCT versus driving current at a distance of 3 cm.*

C. R4125 phototube sensitivity to Infrared light

The main limiting factor for the IR LED based curing system for the NPS can be the small yet remaining PMT sensitivity to infrared light. It is assumed that IR LED curing would be conducted continuously during the experiment without interruption of data taking with the PMT high voltage ON. For such a requirement it is crucial to know:

- at what level the continuous use of an IR LED will change the PMT anode current, and
- if this rise of anode current will have a negative impackt on the PMT linearity, gain, and lifetime.

For all types of PMTs operating in a high background condition (with high rate and/or high anode current) the limiting factors are the lifetime of the photocathode and the gain. Photocathode lifetime is defined by the amount of charge passing between the photocathode and the first dynode after which the PMT quantum efficiency drops by factor ∼2 from its nominal value. The PMT gain-lifetime is defined by amount of total charge passing through anode which results degradation of the PMT gain by a factor of two.

CMS studies show that after some amount of charge collection the PMT characteristics, apart from the gain, do not show any significant change from their values at the start of the measurement: in Ref. [15] the results of a complete test of 2000 Hamamatsu R7525HA phototubes for the CMS forward hadron calorimeter are reported. This is an 8-stage PMT with 25 mm diameter of Bialkali photocathode, with gain $\sim 5 \times 10^5$ at high voltage 1750 V, and typical anode dark current of 5 nA (maximum ∼100 nA). The studies found that the relative drop in the gain after 3000 C of charge collection depends on the High Voltage (or gain) and may vary from ∼2 (at low HV) to 5 (at high HV).

In general, pending on the type of PMT, the photocathode and dynode materials, the mechanical construction and the operation regime, the photocathode-lifetime may well vary from a few tens to a few hundred mC, while the gain-lifetime may vary from few hundred to few thousand C. As a consequence, to prolong the PMT lifetime one needs to keep the cathode and anode currents as low as possible. This is also required for

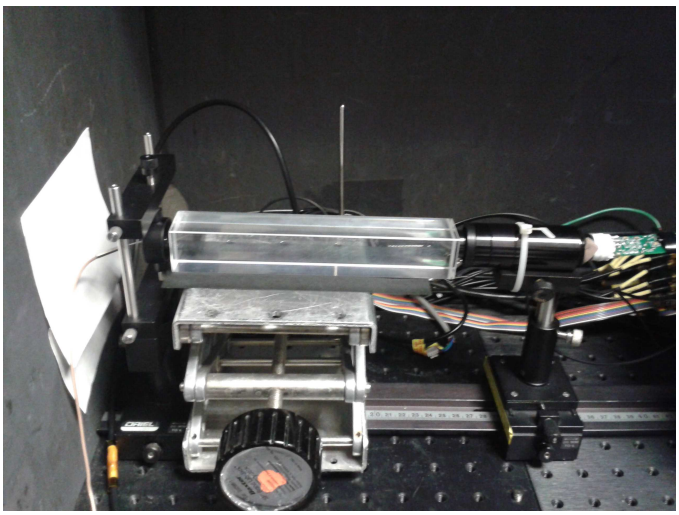

FIG. 6: *Experimental setup for the PMTs sensitivity measurements to infrared light. A 20 cm PbF_2 crystal is installed between the PMT and the LED.*

as minimum as possible dark currents of the PMT. Any additional source which may increase the PMT anode current (dark current) will have a negative impact on the lifetime of the PMT. Thus, curing of the crystals in situ by using a high-intensity infrared light without turning the phototube high voltages off is in practice only possible if the rise of the PMT dark current when the infrared LED is on is completely negligible relative to the anode current, or less than a few times of the nominal dark current.

The possibility to perform continuous curing of the crystal in-situ (with the PMTs' HV on) using infrared light with wavelength $\lambda \geq$900 nm depends thus on the (quantitatively unknown) quantum efficiency of the PMT in this wavelength region. Since effective curing will require a very high IR light intensity ($\geq 10^{17}$ γ/sec) this is even an issue for a small quantum efficiency this IR wave lenght: the phototube could still be completely damaged with such a high intensity IR light.

We thus measured the R4125 phototube's sensitivity to the infrared light. The tube was installed on front of the LED. The measurements were done at different driving currents of the LED (from 0 up to 100 mA), at distances of 0.5 cm and 16 cm (18 cm), with and without a PbF_2 ($PbWO_4$) crystal placed in front of the PMT, and at different gains of the PMT. For these measurements we used one of the prototypes of the active divider with built-in amplifier we developed earlier for this PMT, to increase linearity up to high rates. In the measurements, we first measured single electron peak and gain of R4125. At high voltages of 1600, 1700 and 1750 V, respectively, we found the following gain values: 3.8×10^7; 7.6×10^7 and 1.0×10^8. These values are much higher than those listed in the Hamamatsu data sheet (gain of 10^5 at 1500 V) due to the use of the active divider.

To measure the PMT quantum efficiency at wavelengths far beyond the sensitivity range specified in the Hamamatsu data sheet, in the infrared, the output signal was sent to an ADC, and we used a simple DAQ system based on Lab-VIEW. The ADC gate width was set to be 150 nsec, and a channel was equivalent to 100 fC. Data for each setting were taken for 5 min (300 sec) with a frequency of $\sim$200-300 Hz. Amplitude distributions of the signals were detected at different driving currents through the IR LED LD-274-3 and TSAL7400 type LEDs. We then repeated the measurements with a crystal (PbF_2 or $PbWO_4$) installed between the LED and the PMT, as shown in Fig. 6.

The data suggest that PMT R4125 has a very low, yet not negligible, quantum efficiency relative to infrared light. As example, we show in Fig. 7 the amplitude distributions of the signals detected by the R4125 PMT at different values of the driving currents of the infrared LED NIR LD-274-3. It is possible that the PMT sensitivity may be due to contamination by short wavelength light of the IR LED spectrum. Tests were thus repeated with a 900 nm filter cutting all wavelengths but IR. No difference between the measurements with and

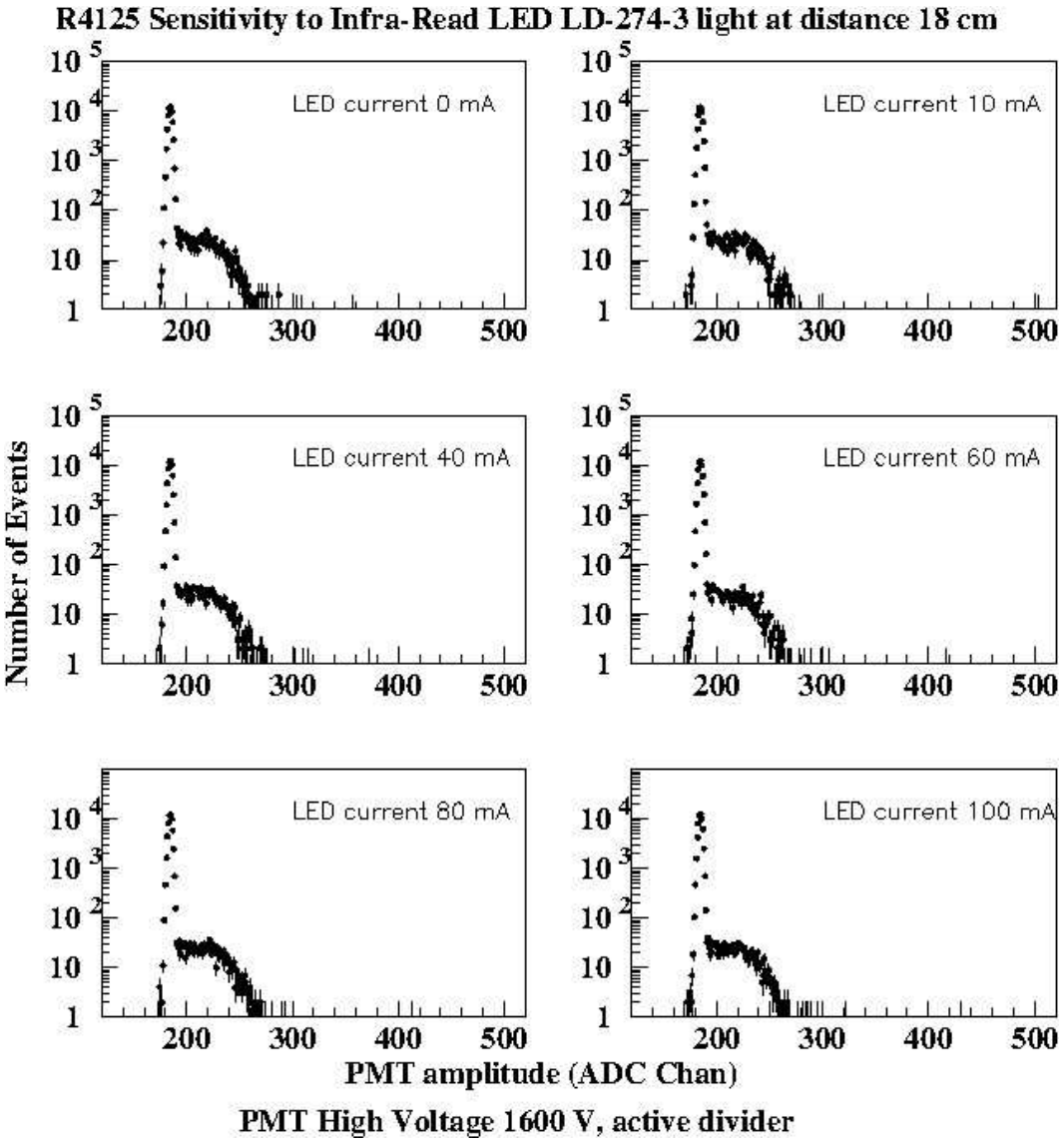

FIG. 7: *The amplitude distributions of the signals detected by PMT R4125 at different values of infrared LED NIR LD-274-3 driving currents.*

without filter were found. This suggests that the majority of the light has IR wave length, that the PMT has a non-zero efficiency with respect to IR light, and that the PMT could thus potentially receive long-term damage if left on during *in situ* IR curing. More studies are ongoing, for instance given the sensitivity to wavelengths $\lambda \geq$900 nm, we may also search for suitable LEDs with an emission spectrum >1000 nm.

To start studying potential damage of the PMT during long-term operation, we measured the PMT R4125 anode current versus driving current of IR LEDs LD-274-3 with the PMT at high voltage settings of 1400 V, 1500 V and 1600 V, respectively, when a single IR LED or a matrix of four IR LEDs illuminated the photocathode. Some results of the measured anode currents with the PMT set at a high voltage of 1600 V are shown in Fig. 8.

With the high voltage of the PMTs on, and no LED driving current, the dark current of the PMT is 11 nA for 1400 V, 18 nA for 1500 V and 28 nA for 1600 V, respectively. Then, for the case where a single LED is positioned at a distance of 19 cm of the front of the PMT, and an LED driving current of 50 mA, the anode current is 309 nA for 1400 V, 492 nA for 1500 V and 758 nA for 1600 V, respectively. For reference, for a similar 50 mA driving current and a matrix of four IR LEDs at this distance, the photon flux would be $\sim 10^{17}\ \gamma/cm^2$/sec. This corresponds to a total charge passing through the PMT due to dark currents of only

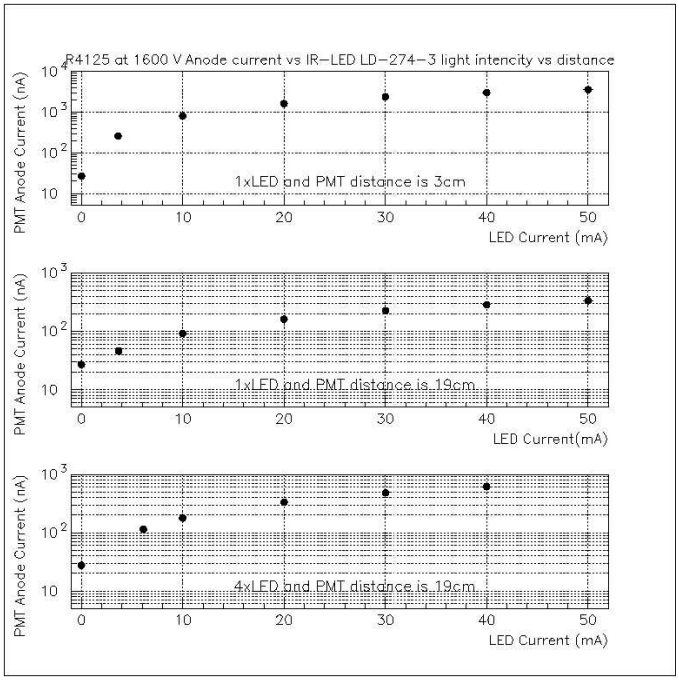

FIG. 8: *PMT anode current, at a high voltage setting of 1600 V, versus the driving current of IR LEDs: (top)- use of one LED positioned at distance 3 cm from the PMT; (middle)- similar, at a distance of 19 cm from the PMT; and (bottom- a matrix of four LEDs at a distance of 19 cm from the PMT*

.

∼3C, for a 1000 hour run (at a high voltage of 1600 V).

The maximum anode current for the R4125 PMT is ∼0.1 mA. The gain of the PMT, using the active divider (with amplifier), is $\sim 3.8 \times 10^7$ at a high-voltage setting of 1600 V. Most likely we will only require a gain in the 10^5 gain range, and not use high voltage settings higher than 1400-1500 V. Thus, there may not be an adverse effect on the PMT, yet it is clear that more study is needed. For the distance of 19 cm, close to the anticipated geometry using ∼18 cm $PbWO_4$ crystals or ∼20 cm PbF_2 crystals sandwiched between the PMT and LED, the PMT dark current values are listed versus the LED driving current in Table 1.

I_{LED} (mA)	I_{Anode} (nA)	I_{LED} (mA)	I_{Anode} (nA)
0.0	27	0.0	27
3.7	46	6.0	114
10.0	92	10.0	177
20.0	161	20.0	334
30.0	225	30.0	478
40.0	284	40.0	609
50.0	332	53.0	758

TABLE I: R4125 phototube anode dark current at an operating high voltage of 1600 V versus the LD-274-3 driving current. The left half of the table illustrates the case when using a single LED, the right half for the case of using a matrix of four LEDs. In each case the PMT was located at a distance of 19 cm from the LED(s).

FIG. 9: *Partly assembled Infrared LED curing system.*

IV. FURTHER STUDIES AND PROTOTYPING

A. Design and construction of the curing system

For further tests we plan to make two versions of the curing system. In the first version, the curing will be performed with a matrix of 4 ultra-bright Blue LEDs per block (with intensity about 10^{16} γ/sec per block). The second version would be a clone of the first one, but with a matrix of 4 ultra-bright Infra-Red LEDs per block (with intensity about 5×10^{17} γ/sec per block). In each case, the matrix of ultra-bright LEDs will be mounted at small distance from the crystals. In Fig. 9 we shown a partly assembled prototype curing system.

B. Irradiation of the $PbWO_4$ crystals

We further plan to do controlled irradiation and curing studies of the various crystals. To this end, we plan to use four $PbWO_4$ crystals, each with dimensions $\sim 1.5 \times 1.5 \times 2.0$ cm^3 for radiation tests. Three of these crystals are passed on to the Jefferson Lab Radiation Control group who have a small facility that can provide controlled doses with a ^{137}Cs gamma source. We plan to irradiate with up to $\sim$20 krad dose each step. The fourth crystal will serve as a reference in the measurements. One of the radiated crystals will be used for tracing spontaneous recovery with time, the two others will be used for curing studies with blue and infrared lights. We plan to monitor the curing effect by intermittent light transmission measurements of the crystals. This work has just started.

C. Prototype Design

Taking into account the possibility of construction of the NPS calorimeter as a combination of $PbWO_4$ and PbF_2 crystals, we have designed a prototype frame that could include both scenarios: a matrix of 3 by 3 $PbWO_4$ crystals, and a matrix for the $PbWO_4/PbF_2$ hybrid case (3 by 2 $PbWO_4$ crystals and 2 PbF_2 crystals. We plan to again use the 19 mm diameter R4125 Hamamatsu PMTs as used in the PrimEx hybrid calorimeter, with our active dividers. We have acquired 10 $PbWO_4$ crystals from SICCAS for our prototype, with quality close to the $PbWO_4$ crystals used by CMS.

D. The Light Monitoring system

A light monitoring system will measure variations of the transmittance of crystals in the course of experiment and provide calibration *in situ*. It will be used to control stability of the detector, degradation of the crystals due to accumulated radiation and define condition when curing of the crystals is needed. It will periodically inject light into the detector modules between the real events during data taking, or during special calibration runs with a frequency 10-20 Hz.

There are three important factors which must be taken into account when considering a light source for the system. First, the source should be as stable as possible. The reference photodiode coupled to it will take out pulse-to-pulse instabilities, but it is still useful to have the primary light source stable in short and long time scale. The second factor is light intensity. Intensity of the light delivered to the large number of crystals in the calorimeter must have an equivalent energy of around 1-3 GeV in each of the crystals. The third factor is timing distribution of the pulses. It must be similar to that from the real event (scintillation pulse for $PbWO_4$ and Cherenkov pulse for PbF_2).

We are studying an LED-based monitoring system to control the status of the $PbWO_4$ blocks and the PMT gains in the course of experiments. The light source is an assembly of NICHINA Super Bright NSPB500AS LEDs located outside of the prototype in radiation safe area. Light from this LED assembly will mix and be delivered to the prototype by ~ 200 μm fiber. There is a special ST type optical fiber connecter on the prototype frame for to plug this primary fiber.

Inside of the prototype box this light will split and delivered to each crystal by bandle of fibers: one monitoring fiber per block. One end of all fibers will be bound together and fed into the ST connector, the second end of the fibers will plug into a hole of an envisioned led-holder plate.

[1] E12-13-010, Exclusive Deeply-Virtual Compton and Neutral Pion Cross Section Measurements in Hall C, Approved by Jefferson Lab PAC40, C. Munoz-Camacho, R. Paremuzyan, T. Horn, J. Roche, and C. Hyde, spokespersons.
[2] E12-13-007, Measurement of the Semi-Inclusive π° Production as Validation of Factorization, Approved by Jefferson Lab PAC40, T. Horn, R. Ent, H. Mkrtchyan, V. Tadevosyan, spokespersons.
[3] Wide-Angle Compton Scattering at 8 and 10 GeV Photon Energies, Deferred proposal by PAC40, updated proposal submitted to PAC42, D.J. Hamilton, S. Sirca and B. Wojtsekhowski, spokespersons.
[4] Initial State Helicity Correlation in Wide Angle Compton Scattering, Proposal submitted to PAC42, D. Day, D. Keller and J. Zhang, spokespersons.
[5] Large Center-of-Mass Angle, Exclusive Photoproduction of π° Mesons at Photon Energies of 5-11 GeV, LOI12-13-003 submitted to PAC40, proposal submitted to PAC42, D. Dutta, H. Gao, M. Amaryan, S. Sirca, I. Strakovsky, spokespersons.
[6] V. Popov, H. Mkrtchyan, New potomultiplier active base for Hall C Jefferson Lab Lead Tungstate Calorimeter, NSSS2012-1098.
[7] Neutral Particle Spectrometer Facility in Hall C, NPS collaboration, https://hallcweb.jlab.org/experiments/PAC40/
[8] M. Kubantsev et al., Performance of the Primex Electromagnetic Calorimeter, arXiv:physics/0609201, 22 Sept. 2006; A. Gasparian, Proceed. X Int. Conf. Calorimetry in Part. Phys., Perugie, Italy, 29 March-2 April 2004, pp. 109-115
[9] M. Anfreville et al., Nucl. Instrum. Meth. A**594**, 292 (2008).
[10] R.W. Nowotny, PANDA Collaboration, IEEE-2009-05402124.
[11] R. Zhu, L. Zhang, Quality of Mass-Produced Lead Tungstat Crystals, IEEE Transact. on Nucl. Science, 51 (2004) 1777-1783
[12] Characterization of Proton Damage in Light-Emitting Diodes, A. H. Johnston and T. F. Miyahira, IEEE Trans. Nuclear Science 47 (2000) 2500-2507
[13] Energy Dependence of Proton Damage in AlGaAs Light-Emitting Diodes, R. A. Reed et al., IEEE Trans. Nuclear Science 47 (2000) 2492-2499
[14] A Precision Measurement of the Neutral Pion Lifetime via the Primakoff Effect, PrimEx Conceptual Design Report, Primex Collaboration, Jefferson Lab, March 3, 2000
[15] Complete Tests of 2000 Hamamatsu R7525HA phototubes for the CMS-HF Forward Calorimeter, U. Akgun et al. Nucl. Instr. Methods, A 550 (2005) 145-156